Parameterization Issues in the Non-Hydrostatic NWP-Model LM

Günther Doms, Almut Gassmann, Erdmann Heise, Matthias Raschendorfer, Christoph Schraff and Reinhold Schrodin

Deutscher Wetterdienst, Abteilung Meteorologische Analyse und Modellierung,
Frankfurter Str. 135, D-63067 Offenbach am Main, Germany

1 Introduction

In December 1999 the Deutscher Wetterdienst (DWD) replaced the old system for numerical weather prediction (NWP) – which comprised a spectral global model GM and two successively nested hydrostatic regional models EM and DM – by a new model suite. The current operational system is made up of the global model GME and the nonhydrostatic limited-area model LM (Lokal-Modell). The global model is a grid-point model with triangular icosahedral mesh for finite differencing on the sphere, and is based on the hydrostatic primitive equations with semi-implicit Eulerian time integration. The LM is a fully compressible nonhydrostatic model utilizing a time integration scheme based on Klemp and Wilhelmson (1978).

The LM was designed as a flexible and portable tool for high-resolution short-range NWP as well as for various research applications using grid-spacings from 50 km down to about 100 m. At present, the model is run operationally for the meso-β scale using a grid spacing of 7 km. Lateron, it is planned to apply the LM for operational forecasts on the meso-γ scale, where nonhydrostatic effects begin to play an essential role in the evolution of atmospheric flows. By employing 2-3 km grid spacing, it is expected that deep moist convection and the associated feedback mechanisms to larger scales of motion can be explicitly resolved. Thus, meso-γ scale NWP models have the potential to overcome the shortcomings resulting from parameterized convection in current coarse-grid models. In particular, a more correct prediction of severe weather events such as supercell thunderstorms, intense mesoscale convective complexes and prefrontal squall-line storms is expected.

To cover both hydrostatic and nonhydrostatic scales of motion, a comprehensive physics package is required. The parameterization schemes have been initially taken from the hydrostatic model DM and adapted to the nonhydrostatic framework. Some fine-tuning was necessary, in particular concerning the cloud-radiation interaction, since a higher horizontal resolution allows for more intense vertical velocities and thus higher cloud water contents. The main efforts, however, concentrated on the development of a new physics package with routines that are believed to have more potential for later use at very high resolution. At present, a new turbulence scheme based on prognostic turbulent kinetic energy, a new surface layer scheme including a viscous sub-layer, a new cloud and precipitation scheme with emphasis on the ice phase, and a multi-layer soil model have been implemented. These schemes are described in some detail and experiences from model applications are discussed.

The development of the LM physics package for small-scale model applications is not yet completed. Other features such as 3-d turbulence, a suitable representation of shallow convection, or the inclusion of hail and graupel in the present microphysics scheme remain to be done. At high spatial resolution, an accurate numerical treatment of dynamical forcings – which drive the physics – was found to become of crucial importance. Errors resulting from an under-resolved topography or from horizontal diffusion in mountainous regions may deteriorate the interaction of physics and

dynamics with a negative impact to the overall solution. For the LM, some remedies such as filtering of topography and a flux-limited horizontal diffusion have been introduced to cope with these problems.

The outline of the paper is as follows. Section 2 gives a short overview of the model formulation, and the LM analysis scheme is described in Section 3. The present operational set-up of the model is briefly summarized in Section 4. The new turbulence scheme and the treatment of the constant-flux layer is outlined in Section 5. In Section 6, the LM cloud ice scheme is described and the impact of advective transport of rain and snow is evaluated. Section 7 considers the shortcomings in the parameterization of deep cumulus convection and examples from using an explicit representation are discussed. The new multi-layer soil model of LM is described in Section 8. The impact of topographical forcing and of horizontal diffusion at high spatial resolution is discussed in Sections 9 and 10, respectively.

2 Model Formulation

Since the LM is a relatively new NWP model, a short summary of both the model formulation and the analysis scheme (Section 3) is included in this paper. More detailed in formation can be found in the model documentation (Doms and Schättler, 1999).

2.1 Differential Form of Model Equations

The regional model LM is based on the primitive hydro-thermodynamical equations describing compressible nonhydrostatic flow in a moist atmosphere. A basic state is subtracted from the equations to reduce numerical errors associated with the calculation of the pressure gradient force in case of sloping coordinate surfaces. The basic state represents a time-independent dry atmosphere at rest which is prescribed to be horizontally homogeneous, vertically stratified and in hydrostatic balance. Thus, the thermodynamic variables temperature (T), pressure (p) and density (ρ) can be formally written as the sum of a height dependent reference value and a space and time dependent deviation, indicated by a prime:

$$T = T_0(z) + T', \qquad p = p_0(z) + p', \qquad \rho = \rho_0(z) + \rho' \,. \tag{1}$$

The base-state variables $p_0(z)$ and $\rho_0(z)$ are determined by specifying a vertical temperature profile $T_0(z)$ and mean sea-level values p_{SL} and T_{SL} for pressure and temperature. The base-state pressure profile then follows from integrating the hydrostatic equation and the base-state density is given by the equation of state. In principle, the reference vertical profile of temperature can be specified arbitrary since we do not linearize the model equations with respect to the reference state. For practical reasons, a constant rate β for the temperature increase with the logarithm of pressure (as proposed by Dudhia, 1993), $\partial T_0 / \partial \ln p_0 = \beta$, is prescribed. Currently, the values $p_{SL} = 1000$hPa, $T_{SL} = 288.15$K and $\beta = 42$K are used for the three parameters specifying the reference state.

The model equations are formulated with respect to a rotated lat/lon-grid with coordinates (λ, φ). In the vertical, we use a generalized terrain-following height coordinate ζ, where any unique function of geometrical height can be used for transformation. Since ζ doesn't depend on time, the $(\lambda, \varphi, \zeta)$-system represents a non-deformable coordinate system, where surfaces of constant ζ are fixed in physical space – in contrast to the pressure based coordinate system of most hydrostatic models, where the surfaces of constant vertical coordinate move in space with changing surface pressure. The transformation of the model equations from the orthogonal (λ, φ, z)-system to the non-orthogonal

terrain-following $(\lambda, \varphi, \zeta)$-system is accomplished by the three elements of the inverse Jacobian matrix $\mathcal{J}^z$,

$$J_\lambda \equiv J^z_{13} = \left(\frac{\partial z}{\partial \lambda}\right)_\zeta, \quad J_\varphi \equiv J^z_{23} = \left(\frac{\partial z}{\partial \varphi}\right)_\zeta, \quad J_\zeta \equiv J^z_{33} = \frac{\partial z}{\partial \zeta} = -\sqrt{G}\,. \tag{2}$$

The terrain-following ζ-system of LM is defined to be left-handed, i.e. with increasing ζ-coordinate for decreasing height z. Thus, J_ζ is always negative and equal the negative absolute value ($\sqrt{G} = |\det(\mathcal{J}^z)|$) of the determinant of the inverse Jacobi matrix. These metrical parameters are not evaluated analytically but numerically on the computational grid. In this way, the model code becomes independent on a specific choice for the terrain-following coordinate. By default, a hybrid Gal-Chen-type coordinate is used.

By transforming the primitive hydro-thermodynamical equations to the (λ, φ, z) coordinate-system and subtracting the basic state, we achieve the following set of prognostic model equations for the three components u, v and w of the wind vector, the perturbation pressure p', the temperature T and the humidity variables q.

$$\begin{aligned}
\frac{\partial u}{\partial t} + \mathbf{v}\cdot\nabla u - \frac{uv}{a}\tan\varphi - fv &= -\frac{1}{\rho a\cos\varphi}\left(\frac{\partial p'}{\partial \lambda} + \frac{J_\lambda}{\sqrt{G}}\frac{\partial p'}{\partial \zeta}\right) + M_u \\
\frac{\partial v}{\partial t} + \mathbf{v}\cdot\nabla v + \frac{u^2}{a}\tan\varphi + fu &= -\frac{1}{\rho a}\left(\frac{\partial p'}{\partial \varphi} + \frac{J_\varphi}{\sqrt{G}}\frac{\partial p'}{\partial \zeta}\right) + M_v \\
\frac{\partial w}{\partial t} + \mathbf{v}\cdot\nabla w &= \frac{1}{\rho\sqrt{G}}\frac{\partial p'}{\partial \zeta} + B + M_w \\
\frac{\partial p'}{\partial t} + \mathbf{v}\cdot\nabla p' - g\rho_0 w &= -(c_{pd}/c_{vd})pD \\
\frac{\partial T}{\partial t} + \mathbf{v}\cdot\nabla T &= -\frac{p}{\rho c_{vd}}D + Q_T \\
\frac{\partial q^v}{\partial t} + \mathbf{v}\cdot\nabla q^v &= -(S^l + S^f) + M_{q^v} \\
\frac{\partial q^{l,f}}{\partial t} + \mathbf{v}\cdot\nabla q^{l,f} + \frac{1}{\rho\sqrt{G}}\frac{\partial P_{l,f}}{\partial \zeta} &= S^{l,f} + M_{q^{l,f}}
\end{aligned} \tag{3}$$

Here, the continuity equation has been replaced by an equation for p'. In Eqs. (3) a is the radius of the earth, c_{pd} and c_{vd} are the specific heat of dry air at constant pressure and constant volume, g is the gravity acceleration, f is the Coriolis parameter, R_v and R_d are the gas constants for water vapour and dry air. ρ is the density of moist air which is calculated as a diagnostic variable from the equation of state:

$$\rho = p\{R_d(1 + (R_v/R_d - 1)q^v - q^l - q^f)T\}^{-1}\,. \tag{4}$$

q^v is the specific humidity, q^l represents the specific water content of a category of liquid water (cloud or rain water) and q^f represents the specific water content of a category of frozen water (cloud ice or snow). The corresponding precipitation fluxes are denoted by P_l and P_f.

The terms M_ψ denote contributions from subgrid-scale processes as, e.g. turbulence and convection and Q_T summarizes the diabatic heating rate due to this processes. The various sources and sinks in the equations for the humidity variables due to microphysical process of cloud and precipitation formation are denoted by S^l and S^f. The calculation of all these terms related to subgrid-scale processes is by physical parameterization schemes. An overview of the schemes used in LM is given is Section 2.4.

The term B in the equation for the vertical velocity is the buoyant acceleration given by

$$B = g\frac{\rho_0}{\rho}\left\{\frac{T-T_0}{T} - \frac{p' T_0}{p_0 T} + \left(\frac{R_v}{R_d} - 1\right) q^v - q^l - q^f\right\}. \tag{5}$$

The advection operator in terrain-following coordinates is defined as

$$\mathbf{v}\cdot\nabla = \frac{1}{a\,\cos\varphi}\left(u\frac{\partial}{\partial\lambda} + v\cos\varphi\frac{\partial}{\partial\varphi}\right) + \dot{\zeta}\frac{\partial}{\partial\zeta},$$

where $\dot{\zeta}$ is the contra-variant vertical velocity in the ζ-system:

$$\dot{\zeta} = \frac{1}{\sqrt{G}}\left(\frac{J_\lambda}{a\cos\varphi}u + \frac{J_\varphi}{a}v - w\right).$$

D is the three-dimensional wind divergence which is calculated from

$$D = \frac{1}{a\cos\varphi}\left\{\frac{\partial u}{\partial\lambda} + \frac{J_\lambda}{\sqrt{G}}\frac{\partial u}{\partial\zeta} + \frac{\partial}{\partial\varphi}(v\cos\varphi) + \cos\varphi\frac{J_\varphi}{\sqrt{G}}\frac{\partial v}{\partial\zeta}\right\} - \frac{1}{\sqrt{G}}\frac{\partial w}{\partial\zeta}.$$

In deriving the prognostic equation for the perturbation pressure from the continuity equation, a source term due to diabatic heating has been neglected. For most meteorological applications, this source term is much smaller than the forcing term by divergence. This approximation is also used in many other nonhydrostatic simulation models. As an additional assumption, the shallow-atmosphere hypothesis has been used.

2.2 Numerical Integration

The model equations (3) are solved numerically using the traditional Eulerian finite difference method. In this technique, spatial differential operators are simply replaced by suitable finite difference operators and the time integration is by discrete stepping using a fixed timestep Δt. The model variables are staggered on an Arakawa-C/Lorenz grid with scalars (temperature, pressure and humidity variables) defined at the centre of a grid box and the normal velocity components defined on the corresponding box faces. For a given grid spacing, this staggering allows for a more accurate representation of differential operators than in the A-grid, where all variables are defined at the same point. In general, we use second order centered finite difference operators for horizontal and vertical differencing.

Because the governing nonhydrostatic equations describe a compressible model atmosphere, meteorologically unimportant sound waves are also part of the solution. As acoustic waves are very fast, their presence severely limits the time step of explicit time integration schemes. In order to improve the numerical efficiency, the prognostic equations are separated into terms which are directly related to acoustic and gravity wave modes and into terms which refer to comparatively slowly varying modes of motion. This mode-splitting can formally be written in the symbolic form

$$\frac{\partial\psi}{\partial t} = s_\psi + f_\psi\,, \tag{6}$$

where ψ denotes a prognostic model variable, s_ψ the forcing terms due to the slow modes and f_ψ the source terms related to the fast acoustic and gravity wave modes. f_ψ is made up of the pressure gradient terms in the momentum equations, the temperature and pressure contributions to the buoyancy term in the w-equation and the divergence term in the pressure and the temperature equation. The subset of equations containing the f_ψ-terms is then integrated with a special numerical scheme.

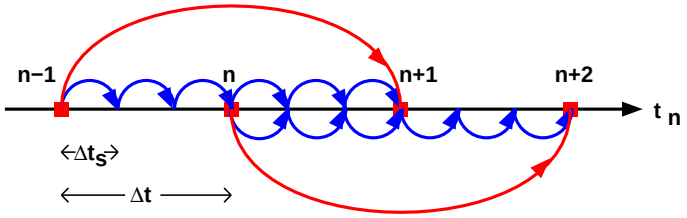

Figure 1: *The time splitting algorithm*

The default time integration method used in LM is a variant of the Klemp and Wilhelmson (1978) scheme including extensions proposed by Skamarock and Klemp (1992). It is based on a Leapfrog integration for the slow modes from time level $n-1$ to time level $n+1$ using an integration interval of $2\Delta t$. The slow mode tendencies are evaluated at time level n for horizontal advection using standard second order centered differences and at time level $n-1$ for most physical forcings. Tendencies from vertical advection and diffusion are calculated by a quasi-implicit scheme. The integration step is then subdivided into a number N_s of small time steps $\Delta\tau_s$ according to $2\Delta t = N_s\Delta\tau$ and the prognostic equations (6) are stepped forward according to

$$\psi^{\nu+1} = \psi^{\nu} + f_{\psi}^{\nu}\Delta\tau + s_{\psi}^{n}\Delta\tau\,. \tag{7}$$

Figure 1 illustrates the basic idea of the time-splitting scheme. In the integration of (7), sound waves are treated explicitly for horizontal directions using the forward-backward method while implicitly for the vertical direction (HE-VI scheme). Thus, the small time step $\Delta\tau$ is limited by the CFL stability criterion for horizontal but not for vertical sound wave propagation. This makes the HE-VI scheme numerically very efficient for large grid aspect ratios, i.e. $\Delta x/\Delta z >> 1$, which are typically used in meso-β and meso-γ applications. An additional 3-D divergence damping as well as a slight time off-centering in the vertical implicit formulation is applied to damp acoustic modes. On the big time step, the Asselin time filter and a 4th-order horizontal diffusion are used for numerical smoothing.

Two alternative time integration schemes have also been implemented for optional use: a two time-level second-order Runge Kutta method based on the work of Wicker and Skamarock (1998), and a three-timelevel Leapfrog-based Eulerian 3-D semi-implicit scheme according to Thomas et al. (2000). These schemes lead to rather similar results in test cases, but have not yet reached operational efficiency.

2.3 Physical Parameterizations

The initial physics package of LM has been adapted from the former operational hydrostatic model DM. It consists of a radiation scheme (Ritter and Geleyn, 1992), a grid-scale cloud and precipitation scheme, a moist convection scheme (Tiedtke, 1989), a soil model (Jacobsen and Heise, 1982), a turbulence scheme based on K-closure, a surface layer scheme after Louis (1979), and a diagnostic scheme to calculate sub-grid scale cloud cover. Meanwhile, a number of new parameterizations have been developed and implemented for optional use, and a part of them is already applied operationally. The new schemes are discussed in Sections 5-8.

2.4 Initial and Boundary conditions

For real data simulations, LM is driven by the new global model GME of DWD using the traditional boundary relaxation technique. A four-dimensional data assimilation cycle based on a nudging

analysis scheme (see Section 3) is provided for operational NWP with the LM. In this case, the initial conditions come from the continuous LM assimilation stream and only boundary data have to be provided by GME forecasts. However, an operational NWP-system can also be set-up without a data assimilation cycle by relying on pure dynamical adaption of large-scale initial fields. In this case, the initial conditions come from interpolated (and initialized) GME analyses. To reduce noise generation and spin-up effects resulting from non-balanced interpolated data, a diabatic digital filtering initialization scheme (Lynch et al., 1997) has been implemented.

For various research applications as well as for model testing and evaluation, the LM provides a capability to handle idealized cases using user-defined artificial initial and boundary data. For these types of application, periodic lateral boundary conditions can be specified optionally. Additionally, a 2-dimensional model configuration can be used.

3 Data Assimilation

The requirements for the data assimilation system for the operational LM are mainly determined by the very high resolution of the model and by the task to employ it also for nowcasting purposes in the future. Hence, detailed high-resolution analyses have to be able to be produced frequently, and this requires a thorough use of asynoptic and high-frequency observations such as aircraft data and remote sensing data. Note that the synoptic scales are largely determined by the lateral boundary conditions provided by the steering model, and the main purpose of the assimilation scheme is to analyze the meso scales.

By design, 3-dimensional analysis methods tend to be less appropriate for this purpose. They do not allow to account for the exact observation time of asynoptic data, and they make it necessary to neglect most of the high-frequent data unless the analysis scheme is applied very frequently at significant computational costs. Moreover, the geostrophic approximation, usually a key ingredient of such schemes, is of limited validity in the meso scale. Therefore, 4-dimensional methods offer potential advantages since they include the model dynamics in the assimilation process directly. Yet, the 4-dimensional variational (4DVAR) method is too expensive for operational application of the LM considering the small amount of time available to produce the analyses and forecasts.

As a result, a scheme based on the observation nudging technique has been developed to define the atmospheric fields. For some of the surface and soil fields, a set of 2-dimensional intermittent analysis schemes is applied in addition. This comprises of the snow analysis, the sea surface temperature (SST) analysis, and the variational soil moisture analysis scheme.

3.1 Nudging-Based Assimilation Scheme

Nudging or Newtonian relaxation consists of relaxing the model's prognostic variables towards prescribed values within a predetermined time window (see e.g. Davies and Turner (1977), Stauffer and Seaman (1990)). In the present scheme, nudging is performed towards direct observations which is more appropriate for high-resolution applications than nudging towards 3-dimensional analyses (Stauffer and Seaman, 1994). A relaxation term is introduced into the model equations, and the tendency for the prognostic variable $\psi(\mathbf{x}, t)$ is given by

$$\frac{\partial}{\partial t}\psi(\mathbf{x},t) \quad = \quad F(\boldsymbol{\psi},\mathbf{x},t) \quad + \quad G_\psi \cdot \sum_{k_{(obs)}} W_k \cdot [\psi_k - \psi(\mathbf{x}_k,t)] \tag{8}$$

F denotes the model dynamics and physical parameterizations, ψ_k the value of the k^{th} observation influencing the grid point $\mathbf{x}$ at time t, $\mathbf{x}_k$ the observation location, G_ψ the constant so-called nudging

coefficient (currently set to $6 \cdot 10^{-4} s^{-1}$ for all assimilated quantities), and W_k an observation-dependent weight which usually varies between 0 and 1. Neglecting the dynamics and physics and assuming a single observation with a constant weight W_k equal 1, the model value at the observation location relaxes exponentially towards the observed value with an e-folding decay rate of $1/G_\psi$ corresponding to about half an hour.

In practical applications, the nudging term usually remains smaller than the largest term of the dynamics so that the dynamic balance of the model is not strongly disturbed. The coupling between the mass and wind field innovations is primarily induced implicitly by the model dynamics. If the assimilation process is successful the model fields will be close to dynamic balance at the beginning of the forecast, and an initialization step is not required.

The factors W_k determine the relative weights given to the different observations at a specific grid point. For a single observation, this weight (w_k) comprises of the quality (and representiveness) of the observation (ϵ_k) and of weights which depend on the horizontal (w_{xy}) or vertical (w_z) distance respectively temporal (w_t) difference between the observation and the target grid point. If an increasing number of observations influence the grid point the total nudging weight should be limited to avoid the nudging term to become dominant over the dynamics. This is achieved by complementing the individual weight w_t by a relative weight (Benjamin and Seaman, 1985):

$$W_k = \frac{w_k}{\sum_j w_j} \cdot w_k \tag{9}$$

$$w_k = w_t \cdot w_{xy} \cdot w_z \cdot \epsilon_k \tag{10}$$

Currently, only conventional observations are used, namely from TEMP and PILOT (temperature and wind (including the significant levels); humidity up to 300 hPa; geopotential only to derive one pressure increment at the lowest model level), AIRCRAFT (all data), and SYNOP, SHIP and DRIBU reports (station pressure; wind for stations below 100 m above msl; humidity; 2-m temperature is used only for the soil moisture analysis). Note that given a cut-off time of 2.5 hours, observations from up to about 2 hours after the actual analysis time can still be assimilated in the first hours of the operational forecast runs. As a quality control, the observed values are compared with the model fields of the assimilating run itself. For multi-level temperature data, a hydrostatic height and thickness check is included, and a spatial consistency check is performed for the station pressure data.

Equation (8) indicates that in principle the scheme consists of two main steps, i.e. the determination of the observation increments and the computation of the weights. With respect to the vertical interpolation required for the first step, the vertical scale of multi-level temperature and wind observations is adjusted to the vertical model resolution by averaging the observed profile over the thickness of model layers. As a result, the simulated thickness between two pressure levels is automatically relaxed towards the observed thickness when nudging temperature data. In contrast, humidity data are interpolated without averaging in order to capture thin layers of clouds as well as possible. Note that the increments are determined as differences in relative humidity which implies that relative rather than specific humidity is relaxed towards the observed humidity. In this sense, the analyzed quantities are horizontal wind, potential temperature, relative humidity, and pressure at the lowest model level.

Related to the second step, incomplete profiles and single-level increments are vertically extended and provided with vertical weights w_z according to a Gaussian (approx.) in log pressure (correlation scale is $1/\sqrt{3}$ for upper-air wind and 0.2 for upper-air temperature and humidity, and the cut-off is 850 m for surface-level wind resp. the lowest model layer for surface-level humidity). Thereafter, upper-air increments are spread laterally along horizontal surfaces since spreading along

the terrain-following model levels as usually applied in nudging-type schemes has disadvantages near steep orography particularly in cases with low stratus (Schraff, 1997). In contrast, surface-level increments are spread along the model levels to limit the area of influence to close to the ground. The spreading includes the computation of the horizontal weights w_{xy} using the function $(1 + \Delta r/s) \cdot e^{-\Delta r/s}$ for the scalar quantities (Δr being the horizontal distance between observation and target grid point). The wind correlations are split into a longitudinal and transverse part, and this allows to specify the degree of divergence (γ) of the resulting wind analysis increment field (Lorenc et al., 1991). Both the correlation scales s and the non-divergence factor γ increase with height and with distance to the observation time and vary between about 60 km and 160 km resp. 0.4 and 0.7 . The function used for the temporal weights w_t is 1 at the observation time and decreases linearly to zero at 3 hours (for radiosonde data) resp. 1.5 hours (for other data) before and 1 resp. 0.5 hours after the observation time. Hourly or more frequent data are linearly interpolated in time.

In the current scheme, the resulting analysis increment fields are partly balanced explicitly in a third major step before being added to the model fields. Three types of balancing are applied. First, a hydrostatic upper-air temperature correction balances the pressure analysis increments at the lowest model layer. It is nearly constant within the lowest 1500 m (therefore hardly modifies the stability within the boundary layer) and decreases rapidly further above such that the geopotential above 400 hPa is not directly modified by the surface pressure nudging (for hydrostatic conditions). This significantly reduces the vertical extent of the mass field disturbance imposed by the pressure nudging and results in a better adjustment of the wind field and a greatly improved assimilation of the pressure data. Secondly, a geostrophic wind correction partly balances the wind field with respect to the mass field increments imposed by the surface pressure nudging including the temperature correction. Finally, an upper-air pressure correction balances the total analysis increments of the mass field hydrostatically. This is the only feature directly related to the fact that the model is non-hydrostatic. Note that it does not change the non-hydrostatic properties of the full model fields. The correction prevents the introduction of direct sources of vertical wind for which there is no direct control without vertical wind observations being available to be assimilated. This is important since the vertical velocity is still small on the scales to be analyzed with the current scheme and observations (in contrast e.g. to a latent heat nudging scheme).

3.2 SST, Snow Depth, and Soil Moisture Analysis

Since the latent and sensible heat fluxes over water depend crucially on the surface temperature, a sea surface temperature (SST) analysis is performed once per day. Starting from the previous analysis as first guess, all the ship and buoy observations from the previous 6 days are used in a correction scheme based on Cressman-type weighting. In data-poor areas, this is blended (via the global SST analysis) with a daily 1° x 1° SST analysis from NCEP which also incorporates satellite data. For the sea-ice cover in the Baltic Sea, an external analysis (from the Bundesamt fuer Seeschiffahrt und Hydrologie) is used.

The occurrence of a snow cover strongly influences the radiative absorption and reflection properties of the land surface and therefore the screen-level temperature. The snow water content is a prognostic quantity of the model, and is analyzed once every 6 hours. The method is based on a simple weighted averaging of SYNOP snow depth observations. The weighting depends both on the horizontal and vertical distances to the target grid points. In areas, where the density of these data is not sufficient, an average of snow depth increments derived from SYNOP precipitation, temperature, and weather reports as well as the model prediction are also included.

In land areas without snow, screen-level temperature (and humidity) is significantly influenced by

the soil water content on clear-sky days. An inadequate specification of soil moisture can lead to forecast temperature errors of several degrees. The variational analysis scheme (Hess, 2001) derives improved moisture contents once per day by minimizing a cost functional J which depends on the deviations of the forecast temperature $T(\eta)$ from the observed (resp. analyzed) temperature T^o and of the soil moisture η from a given background state η^b:

$$J(\eta) \quad = \quad \frac{1}{2}\Big(T^o - T(\eta)\Big)^T \mathbf{R}^{-1}\Big(T^o - T(\eta)\Big) + \frac{1}{2}\Big(\eta - \eta^b\Big)^T \mathbf{B}^{-1}\Big(\eta - \eta^b\Big) \tag{11}$$

The observation error covariance $\mathbf{R}$ and background error covariance $\mathbf{B}$ reflect the trust in the observations resp. the background. To solve the minimization problem, two assumptions are made. Firstly, since the 2-m temperature mainly depends on the soil moisture at the same location, the problem can be decoupled horizontally, and a low-dimensional (equal to the number of analyzed soil layers) minimization can be performed for each grid point individually. Secondly, (moderate) changes of soil moisture are assumed to lead to linear changes in temperature. This allows to derive the linear relationships $\mathbf{\Gamma}$ by means of one additional forecast run per analyzed soil layer where each of these forecasts has slightly different values for the initial soil moisture. The minimum of J can then be found by solving $\nabla J(\eta) = 0$ directly without using the adjoint method.

In the current implementation, two additional 15-hour forecasts are required to analyze two (sets of) soil layers for 0 UTC of the previous day by comparing forecast and observed temperature at 12 and 15 UTC. The analysis increments are then added to the soil moisture of the 0 UTC nudging analysis of the current day. The resulting soil moisture is used both as initial state for the operational LM forecast of the current day and as background state for the next soil moisture analysis. This background state η^b is important in order to reduce the daily variation of the soil moisture contents and to stabilize the minimization in cases of weak soil-atmosphere coupling (i.e. cloudy situations). Together with η^b (see above), the background error covariance $\mathbf{B}$ for the following day is provided in a Kalman-filter cycled analysis:

$$(\mathbf{B})^{next} \quad = \quad \mathbf{A} \; + \; \mathbf{Q} \quad , \quad \textit{where} \;\; \mathbf{A} = (\nabla^2 J)^{-1} = \Big(\mathbf{\Gamma}^T \mathbf{R}^{-1} \mathbf{\Gamma} + \mathbf{B}^{-1}\Big)^{-1} \tag{12}$$

This takes into account both an increase of confidence in the retrieved soil moisture values due to the utilized screen-level observations (as part of the analysis error covariance $\mathbf{A}$) and a decrease of confidence due to the model error $\mathbf{Q}$ of the soil model. While $\mathbf{A}$ can be computed explicitly, $\mathbf{Q}$ is the main tuning parameter of the scheme. It influences the relative weight given to the past and the present observations and has an impact on the temporal variability of the soil moisture.

4 Operational Application and Verification

The LM is operated in four meteorological centres of the *Consortium for Small-Scale Modelling* (COSMO), which comprises the four national weather services DWD, HNMS (Hellenic National Meteorological Service, Greece), MeteoSwiss (Switzerland) and UGM (Ufficio Generale per la Meteorologia, Italy), the regional service ARPA-SMR (Il Servizio Meteorologico Regionale di ARPA, Italy) and the AWGeophys (Amt für Wehrgeophysik, Germany). The COSMO group aims at the development, improvement and maintenance of an operational non-hydrostatic limited-area modelling system based on the LM.

Figure 2 shows the integration domains of the operational model runs at DWD, MeteoSwiss, HNMS and ARPA-SMR. All members use a 7 km grid spacing and a 40 sec time step except HNMS ($\Delta s =$ 14 km and $\Delta t = 80$ sec). In Switzerland, a 45-layer version of the model is integrated whereas all other centres use 35 layers by default. Boundary conditions are interpolated from forecasts of the

global model GME at DWD and are updated at hourly intervals. HNMS and ARPA-SMR start the LM forecasts from interpolated GME analyses. At DWD and MeteoSwiss a four-dimensional data assimilation suite based on nudging analysis has been installed. The forecast range is 48 hrs at all centres.

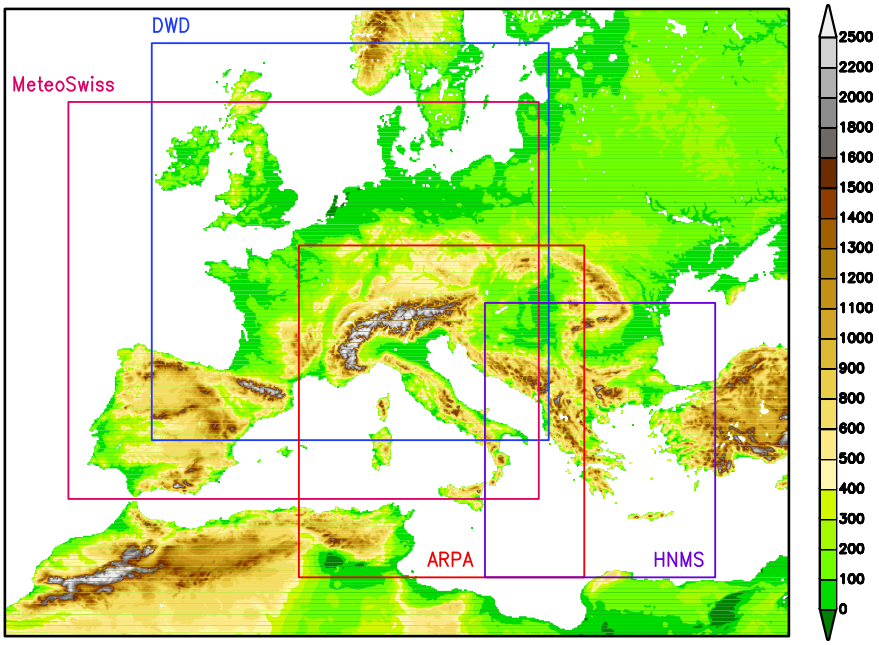

Figure 2: LM integration domains at DWD, MeteoSwiss, ARPA-SMR and HNMS

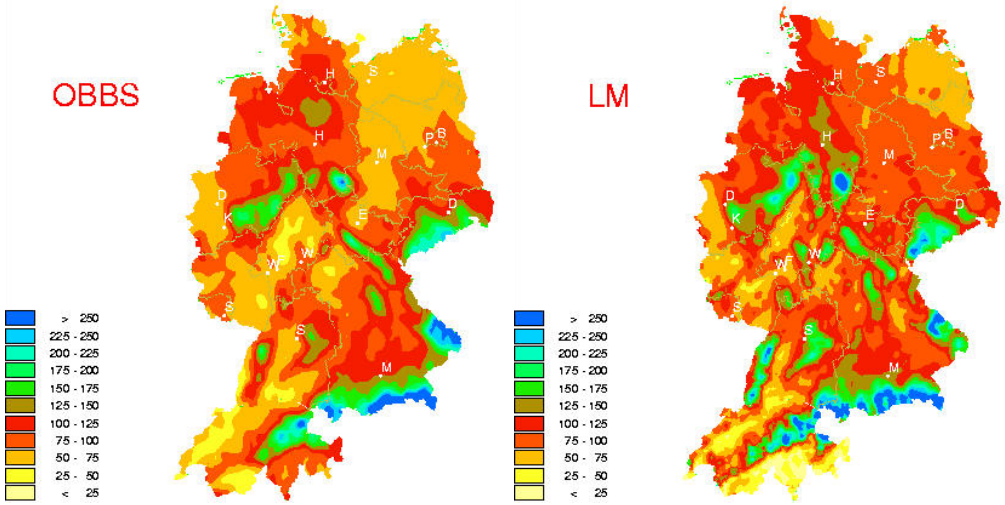

Figure 3: Monthly precipitation sum (mm) for March 2000 as observed (OBBS) by climate networks (max: 481 mm, mean: 103mm) and derived from 00 UTC LM forecasts at DWD (max: 995 mm, mean: 103mm).

The operational verification of the model forecasts at the centres is by standard methods and is mostly based on coarse SYNOP and TEMP observations. Verification scores are derived on a daily, monthly and quarterly basis and are exchanged within the COSMO group. An overview of various verification products is given in the COSMO Newsletter (2001). For precipitation, also regional

high-resolution observation networks are used. As an example, Fig. 3 shows the distribution of monthly precipitation amounts for March 2000 as obtained from the climate networks of DWD and MeteoSwiss (about 5000 stations) and from the corresponding 00 UTC LM runs at DWD. Most details resulting from orographical forced enhancement of precipitation are well represented by the LM forecasts, e.g. the high rain amounts along the northern ridge of the Alps, over the Black Forest and over various low mountain ranges in Germany and along its southeastern border. In most of these mountainous areas, however, the peak values are overestimated. Other verification results also reveal that the predicted precipitation patterns are not very satisfactory over regions with steep topography. The impact of topography on high-resolution precipitation forecasts will be discussed in Section 9 and 10.

5 A New TKE-Based Scheme for Vertical Diffusion and Surface-Layer Transfer

The LM standard scheme for vertical turbulent transport is based on a second-order closure at hierarchy level 2.0 (Mellor and Yamada, 1974), resulting in a traditional diagnostic K-closure. For the Prandtl-layer, a stability and roughness-length dependent surface flux formulation according to Louis (1978) is applied. Results from verification and model diagnostics, however, reveal a number of drawbacks:

- There is often insufficient vertical mixing in case of stable stratification during nighttime. This results in too cold and too shallow inversion layers, with a tendency for a decoupling of the surface and the lower atmosphere.
- Also, at the top of the boundary layer there is insufficient mixing in many cases. Here, stratiform PBL (planetary boundary layer) clouds tend to disperse too slowly.
- The scheme gives no solution for large Richardson numbers exceeding a critical value. Thus, there is almost no physical mixing above the boundary layer, which contributes to a too weak PBL entrainment.
- No distinction is made between the values of variables at the surface and in the roughness height z_0. This results in a too small diurnal cycle of surface temperature and too strong evaporation from bare soils.

Instead of searching for remedies within the diagnostic K-closure, a new scheme based on prognostic turbulent kinetic energy (TKE) has been developed. Specific features of the scheme are: (i) formulation in terms of liquid water potential temperature and total water content, (ii) inclusion of subgrid thermal inhomogeneities and (iii) application of a generalized averaging operator to include the interaction of the flow with solid obstacles (roughness elements such as trees or buildings) within a grid box. The latter option, however, is not applied operationally. The parameterization of surface-layer fluxes has also been completely reformulated in the framework of the TKE-scheme. Some details on the new turbulence formulation are described in the following subsections.

5.1 General Concept

The vertical diffusion scheme is based on the second order moments of the basic equations. In deriving these equations, however, a more general averaging operator is used which takes solid roughness elements within a control volume (the grid box volume) into account. This method has

first been introduced by Raupach and Shaw (1981) for canopy-layer flow. Let V_0 be the volume of a rectangular control box, and $r_V = V/V_0$ the volume fraction which is filled with air (the remaining portion is filled with solid obstacles). Averaging is then done by a running volume mean (denoted by an overbar in the following) only for the part V of V_0. For the generic budget equation for a mass-specific quantity ψ,

$$\frac{\partial \rho\psi}{\partial t} + \nabla \cdot (\rho \mathbf{v}\psi - a^{\psi}\nabla\psi) = Q_{\psi}\,, \tag{13}$$

where a^{ψ} is the molecular diffusion constant and Q_{ψ} is the source function, the following form of filtered budget equations results:

$$\frac{\partial \overline{\rho}\widehat{\psi}}{\partial t} + \nabla \cdot (\overline{\rho}\widehat{\mathbf{v}}\widehat{\psi} + \mathbf{F}^{\psi} - a^{\psi}\nabla\overline{\psi}) + (R^{\psi}_{vol} + R^{\psi}_{mol}) = \overline{Q}_{\psi}\,. \tag{14}$$

Here, the mass-weighted mean $\widehat{\psi} = \overline{\rho\psi}/\overline{\rho}$ with the corresponding turbulent fluctuation $\psi'' = \psi - \widehat{\psi}$ is used for mass-specific variables. $\mathbf{F}^{\psi} = \overline{\rho \mathbf{v}''\psi''}$ denotes the mean turbulent flux. Two additional terms appear in (14) which are related to body-air interactions: A volume term R^{ψ}_{vol} describing the impact of spatial variations of the air-fraction r_V, and a surface term R^{ψ}_{mol} which takes molecular fluxes to the solid body surfaces into account. They are defined by

$$R^{\psi}_{vol} = (\overline{\rho}\widehat{\mathbf{v}}\widehat{\psi} + \mathbf{F}^{\psi} - a^{\psi}\nabla\overline{\psi}) \cdot \nabla(\ln r_V)\,, \tag{15}$$

$$R^{\psi}_{mol} = \frac{1}{V}\int_S (a^{\psi}\nabla\psi) \cdot \mathbf{n}\, dS\,, \tag{16}$$

where in (16) the integration is along the solid body surface S and $\mathbf{n}$ is the unit vector perpendicular to the surface. Using (13) and (14), the derivation of the second order moments, i.e. the budget equations for the turbulent fluxes, is straightforward. The resulting equations, however, will contain additional volume and surface terms corresponding to (15) and (16). A special example of a 2-nd order equation is the budget of turbulent kinetic energy (TKE) $e_t = \mathbf{v}'' \cdot \mathbf{v}''/2$:

$$\frac{\partial \overline{\rho}\widehat{e_t}}{\partial t} + \nabla \cdot (\overline{\rho}\widehat{\mathbf{v}}\widehat{e_t} + \mathbf{F}^{e_t} - \mu\overline{\mathbf{v}'' \cdot \nabla\mathbf{v}}) + (R^{e_t}_{vol} + R^{e_t}_{mol}) = -\overline{\mathbf{v}'' \cdot \nabla p} - \overline{\rho \mathbf{v}''\mathbf{v}''} \cdot\cdot \nabla\widehat{\mathbf{v}} - \varepsilon\,. \tag{17}$$

The volume and surface term are given in a similar way as in (15) and (16), and the dissipation rate is denoted by $\varepsilon = \mu\overline{\nabla\mathbf{v}'' \cdot\cdot \nabla\mathbf{v}}$, where μ is the dynamic viscosity. In the TKE-equation (17), the pressure correlation term may be expanded into

$$-\overline{\mathbf{v}'' \cdot \nabla p} \simeq -\frac{1}{\overline{\rho}\overline{\theta}_v}\mathbf{F}^{\theta_v} \cdot \nabla\overline{p} + \widehat{\mathbf{v}} \cdot \overline{\nabla p'} \tag{18}$$

θ_v is virtual potential temperature and $\mathbf{F}^{\theta_v} = \mathbf{F}^{\theta} + \{1 + (R_v/R_a - 1\}\mathbf{F}^{q_v} - \mathbf{F}^{q_c}$ denotes the buoyant heat flux, which is comprised of the turbulent heat flux $\mathbf{F}^{\theta}$, the flux of specific humidity $\mathbf{F}^{q_v}$ and the flux of specific cloud water content $\mathbf{F}^{q_c}$. The second term in the pressure work function (18) represents the formation of TKE due to wake production from obstacles within the flow. Note that the generalized averaging operator does not commute with respect to partial spatial differentiation (i.e. $\overline{\nabla p'} \neq \nabla\overline{p'} = 0$). For $\overline{\nabla p'}$, the well know isotropic form-drag parameterization is applied.

For the derivation of the second order budgets, it is sufficient to use a somewhat simplified set of basic model equations: Coriolis forces, radiation and precipitation are not considered since the direct impact of these processes on turbulent fluxes is negligible. In order to avoid source term correlations, it is also convenient to apply a thermodynamically filtered set of equations where the phase transition rate due to cloud condensation/evaporation does not occur explicitly. This is achieved by transforming from (θ, q_v, q_c) to liquid water potential temperature $\theta_l = \theta - (L_V/c_{pd})q_c$ and total water $q_w = q_v + q_c$ as dependent variables. Both θ_l and q_w are conserved during moist

adiabatic vertical displacements. The resulting second order moments will provide relations for the turbulent fluxes of θ_l and q_w. In order to recover the turbulent fluxes $\mathbf{F}^{\theta}$, $\mathbf{F}^{q_v}$ and $\mathbf{F}^{q_c}$ – which are required by the original model equations – from the fluxes $\mathbf{F}^{\theta_l}$ and $\mathbf{F}^{q_w}$ of the second order scheme, a closure condition for phase transitions is required to relate the variables (θ, q_v, q_c) in a unique way to (θ_l, q_w). We use a variant of the statistical cloud scheme of Sommeria and Deardorff (1977) for this purpose. By this scheme, fluctuations in the thermodynamic variables are no longer independent, but become coupled through instantaneous condensation or evaporation of cloud water. This results in an equivalent coupling of the corresponding fluxes. For instance, the buoyant heat flux in (18) is given by a linear relation between $\mathbf{F}^{\theta_l}$ and $A_q\mathbf{F}^{q_w}$,

$$\mathbf{F}^{\theta_v} = A_\theta \mathbf{F}^{\theta_l} + A_q \mathbf{F}^{q_w}\,, \tag{19}$$

where the factors A_θ and A_q depend on the saturation fraction r_c of a grid volume. r_c may be interpreted as the fractional cloud cover and is also diagnosed by the scheme. Similar linear relations hold for the calculation of $\mathbf{F}^{\theta}$, $\mathbf{F}^{q_v}$ and $\mathbf{F}^{q_c}$ in terms of $\mathbf{F}^{\theta_l}$ and $\mathbf{F}^{q_w}$. The major advantage of this approach is a consistent inclusion of the effects from sub-grid scale condensation on the turbulent fluxes of heat and moisture.

5.2 An Extended level 2.5 Scheme for Vertical Diffusion

For the 5 model variables u, v, w, θ_l, and q_w, the budgets for the corresponding second order moments build a set of 15 prognostic equations. To arrive at a tractable version, a closure on level 2.5 (in the notation of Mellor and Yamada, 1982) is applied. That is, local equilibrium is assumed for all moments except for TKE, where advection and turbulent transport is retained. Furthermore, Rotta-type relaxation approximations (return-to-isotropy) for the pressure covariance terms and Kolmogorov-Heisenberg closure conditions for the dissipation terms are utilized (see e.g. Stull, 1988). The boundary layer hypothesis of horizontal homogeneity is applied as usual, since effects from 3-D turbulence can be neglected for the present meso-β application of the model (these will be incorporated lateron). This leaves only vertical fluxes in the system of equations, where – with the help of the Boussinesq approximation – the difference between the mass-weighted and the Reynolds averages becomes obsolete: $\overline{\rho w''\psi''} \simeq \overline{\rho}\,\overline{w'\psi'}$. We arrive at a set of second order equations with a flux-gradient representation for the turbulent fluxes in the form

$$\overline{w'\psi'} = -K^H \frac{\partial \overline{\psi}}{\partial z}\,, \quad K^H = q\lambda S^H\,, \quad \text{for } \psi = \theta_l, q_l \tag{20}$$

$$\overline{w'\psi'} = -K^M \frac{\partial \overline{\psi}}{\partial z}, \quad K^M = q\lambda S^M, \quad \text{for } \psi = u, v \tag{21}$$

where the turbulent diffusion coefficients for heat (K^H) and momentum (K^M) are computed in terms of corresponding stability functions for scalars (S^H) and for momentum (S^M), of the turbulent length scale λ and of the turbulent velocity scale $q = \sqrt{2\overline{e_t}}$. The stability functions are determined by a set of two linear equations. For λ, the Blackadar mixing length is assumed and q is predicted using the TKE-equation in the form

$$\frac{\partial q^2}{\partial t} + \overline{\mathbf{v}} \cdot \nabla q^2 - \frac{1}{\overline{\rho}}\frac{\partial}{\partial z}\left(\alpha_T \overline{\rho}\lambda q \frac{\partial q^2}{\partial z}\right) = 2K_M\left\{\left(\frac{\partial \overline{u}}{\partial z}\right)^2 + \left(\frac{\partial \overline{v}}{\partial z}\right)^2\right\} + \frac{2g}{\overline{\theta}_v}\overline{w'\theta_v'} - \frac{q^3}{\alpha_M \lambda}\,. \tag{22}$$

Here, α_M and α_T are model constants related to the parameterization of the dissipation term and the flux-gradient representation of the turbulent TKE-transport, respectively. According to (19) and (20), the buoyant heat flux in (22) is given by

$$\overline{w'\theta_v'} = -K_H \Gamma_v\,, \quad \text{with} \quad \Gamma_v := A_\theta \frac{\partial \overline{\theta}_l}{\partial z} + A_q \frac{\partial \overline{q}_w}{\partial z}\,. \tag{23}$$

Γ_v denotes the effective gradient of virtual potential temperature. For dry conditions (cloud fraction $r_c = 0$), Γ_v is given by the gradient of potential temperature, whereas for moist saturated conditions (cloud fraction $r_c = 1$) Γ_v is given by the gradient of equivalent potential temperature. Thus, with increasing cloud fraction r_c, the state of neutral thermal stability is gradually shifted from dry adiabatic to moist adiabatic stratification. Thereby, higher in-cloud values of turbulent kinetic energy and the corresponding increased vertical mixing in case of a stratocumulus topped boundary layer are taken into account. Also, cloud-top entrainment will be simulated directly without a need for further parameterizations.

Besides the inclusion of sub-grid scale condensation, there are two major extensions compared to traditional level 2.5 schemes. The first is a consistent representation of interactions of the flow with solid obstacles within a grid volume, both in the grid-scale equations and in the second order equations. This concept is useful for various research purposes and allows for instance to resolve canopy layer flows explicitly (flow through porous media). In the current operational application of the model, however, this option is not used and it will not be described further. The second extension concerns the inclusion of subgrid thermal circulations. Inhomogeneities at the rigid surface will always give rise to differential heating and cooling resulting in direct thermal circulation patterns of a length scale being smaller than the grid scale but larger than that of small-scale turbulence. In such a situation, there will be a conversion of kinetic energy related to the circulation patterns (CKE) into TKE with a positive definite source term. This process will especially prevent the solution of the TKE-equation to tend to zero in case of very stable thermal stratification and an the well known but unrealistic decoupling of the atmosphere and the surface can be avoided.

The key to get a formulation of this additional source term is the separation of the total sub-grid scale spectrum of motion into a small-scale turbulent part and a large-scale part associated with the thermal circulations. The covariance of two variables may then be decomposed

$$\overline{\phi'\psi'} = (\overline{\phi'\psi'})_L + (\overline{\phi'\psi'})_S \tag{24}$$

into a corresponding large-scale part $(...)_L$ and a small-scale turbulent part $(...)_S$. Using this decomposition, it is possible to derive 2nd-order budgets for both parts separately. Formally, those band pass budgets differ from the total budgets only by conversion terms describing scale interactions of the circulation and the turbulent scales of motion. With a number of approximations and simplifications, it can be shown that the additional source term in the TKE equation is mainly formed by the large scale part of the buoyant heat flux. The simplified equations provide the relation

$$(\overline{w'\theta'_v})_L \propto \tau_L \frac{g}{\overline{\theta}_v}\overline{\theta'^2_v} \propto -\tau_L^2 \frac{g}{\overline{\theta}_v}\frac{\partial(\overline{\rho}\overline{w'\theta'^2_v})_L}{\overline{\rho}\partial z}\,, \tag{25}$$

where τ_L is the circulation time scale. This relation is obtained by considering the 2nd order large-scale budget of temperature variance only. Due to thermal inhomogeneities at the rigid surface, temperature variance will always be generated near the surface and then be transported into the atmosphere. According to (25), the large-scale heat flux is positive definite. Even in a stable boundary layer it is always directed upwards, but it will be over-compensated by the downward small-scale turbulent fluxes near the surface. The vertical integral of the total heat flux, however, will remain (slightly) positive, which gives the desired impact in the TKE equation. In the present version of the scheme, we use the following parameterization for the large-scale heat flux:

$$(\overline{w'\theta'_v})_L = -L_{pat}\left(\frac{\lambda}{q}\right)^2 \frac{g}{\overline{\theta}_v}\frac{\partial(\overline{\rho}K_H\Gamma_v^2)}{\overline{\rho}\partial z}\,. \tag{26}$$

L_{pat} is a pattern length scale representing the dominant scale of thermal inhomogeneities at the surface. Currently, L_{pat} is given a fixed value of 500 m for the model grid spacing of 7 km. Lateron,

this value will be replaced by a location dependent external parameter field. The large-scale heat-flux parameterized by Eq. (26) is added to the small-scale one in (23) to give the total subgrid-scale heat flux used in the TKE equation (22). Examples on the impact of the subgrid-scale thermal circulations are discussed in Section 5.4.

5.3 The Surface Transfer Scheme

The new LM surface-layer scheme is intimately related to the TKE scheme described above. Here, the surface layer is defined to be the layer of air between the earth surface and the lowest model level. We subdivide the surface layer into a laminar-turbulent sub-layer, the roughness layer, and a constant-flux or Prandtl layer above. The roughness layer extends from the non-planar irregular surface, where the turbulent distance $l = \lambda/\kappa$ (λ is the turbulent length scale and κ is the von Karman constant) is zero, up to a level $l = H$, such that l is proportional to the vertical height z within the Prandtl layer above. We choose H to be equal to the dynamical roughness length z_0. The lower boundary of the constant-flux layer (and of the atmospheric model) is defined to be a planar surface at a turbulent distance $l = H$ from the surface. This subdivision allows to discriminate between the values of the model variables at the rigid surfaces (predicted by the soil model) and values at the level $l = H$, which are 'seen' by the atmosphere.

For both layers, the fluxes are written in resistance form, where a roughness layer resistance is acting for scalar properties but not for momentum. Specific interpolation schemes are used to calculate the transport resistances of the layers. The new surface scheme does not make use of empirical Monin-Obukhov stability functions, rather it generates these functions by the use of the dimensionless coefficients of the Mellor-Yamada closure and the interpolation rules. As the Mellor-Yamada closure has been comprehensively tested in numerous applications, the estimates of its coefficients are fairly reliable. This tends to reduce the number of LM model parameters to be tuned. However, a number of additional model parameters and external parameters related to the roughness layer have been introduced. They describe the impact of various types of the underlying surface on the vertical profiles functions and the transport resistances of momentum, heat and moisture in more detail. These parameters have been tuned in a number of parallel runs.

5.4 Results and Experiences

To investigate the impact of the thermal circulation term (26) in the new turbulence scheme, single column simulations were performed. These simulations were driven by observed temperatures and dew points at 2 m height in order to exclude interactions with the surface layer scheme and the soil model. The simulations started with vertical profiles obtained by radio soundings at midnight. All measurements are taken from the Lindenberg observatory of DWD and the external parameters are specified for this area. The simulations were performed for a high pressure situation in July 1997 with weak advection, so that the single column simulations are comparable with data from measurements.

Fig. 4 shows the initial profile of potential temperature (Tet) at 00 UTC (hour = 0) and the observed (mes) and simulated profiles after 18 and 24 hours. The left picture shows the simulation without using the circulation term ($L_{pat} = 0m$) and the picture to the right shows the case with $L_{pat} = 2000m$. The observations indicate the transition of an initially stable boundary layer into a well mixed layer, which is fully established at 18 UTC. Afterwards, the stable stratification is re-established. Both model versions simulate the formation of the well mixed layer. The reformation of the stable boundary layer during nighttime, however, is very different. Obviously, in the first case the model simulation results in a very shallow inversion layer with neutral stratification above.

This is not in accordance with the observations. By including the the circulation term, the model simulation is able to reproduce the measured shape of the inversion fairly well. A comparison of time series from the model runs and the observations (not shown) does also reveal that the amplitude of the diurnal cycle of temperature in about 300 m height is underestimated by the simulation without the circulation term, but is well reproduced by including this term. During nocturnal cooling, it is this additional TKE production term that makes the cold air at the surface to be mixed more efficiently with air at higher levels.

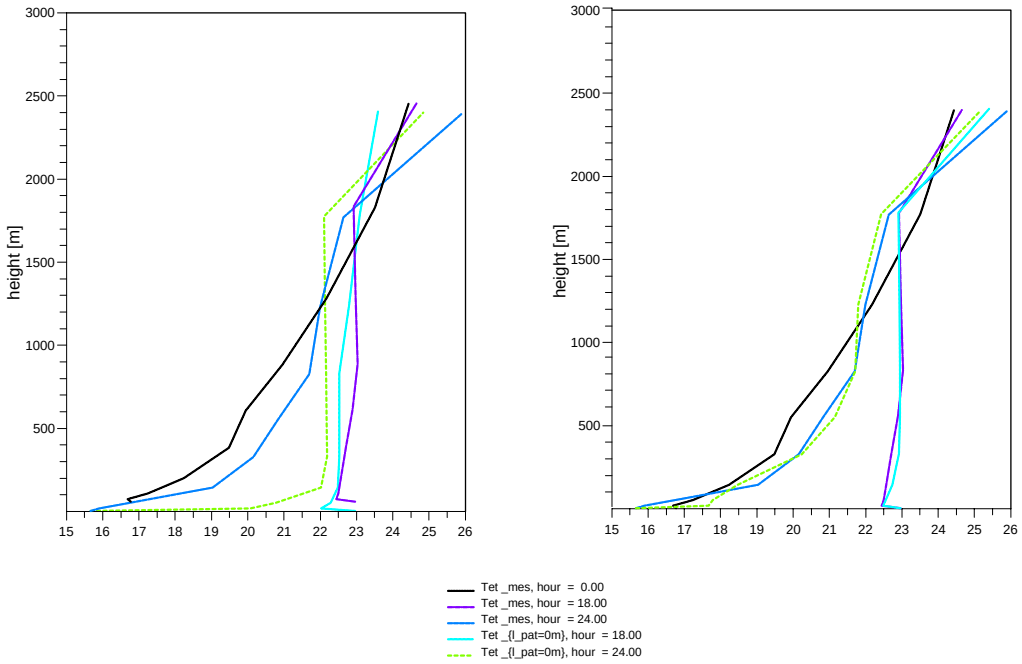

Figure 4: 1-D boundary layer simulation for 10 July 1997 at Lindenberg. Left: simulation without the circulation term. Right: simulation including the circulation term.

As an example of a full 3-D LM simulation with the new TKE-scheme (including the circulation term), Fig. 5 illustrates some results from a 12 hour forecast starting at 00 UTC on 22 July 1999. In this case, a low pressure situation over France and Germany prevailed which was associated with a upper level trough. Fig. 5 shows west-east cross sections for horizontal wind speed (top left), potential temperature (top right) and TKE at about 48° geographical latitude. The wind speed chart shows two jet maxima corresponding to the western and eastern flanks of the trough. This jet stream structure is reproduced by both the new turbulence scheme and the old diagnostic K-closure. Although the new version generates more mixing at stable stratification, the jet stream is completely retained. The lower panel in Fig. 5 shows the TKE fields obtained from the model run using the prognostic TKE-scheme (left) and from the reference run using the old scheme (right). Due to the stable stratification (see upper right picture of Fig. 5), the old scheme gives just a small background value for TKE in the middle and higher troposphere, which is related to a prescribed minimum diffusion coefficient. This background value is exceeded only in a few discrete regions, where the Richardson number is less than its critical value.

The new scheme, however, is able to simulate some realistic structures of the TKE field in the upper troposphere. There are two local TKE maxima belonging to the upper and lower edge of each of both jet maxima, where strong vertical gradients of horizontal velocity occur, which contribute to the generation of strong turbulence. But at the western jet maximum, the upper region of large vertical velocity gradients is within a region of strong stable stratification. This

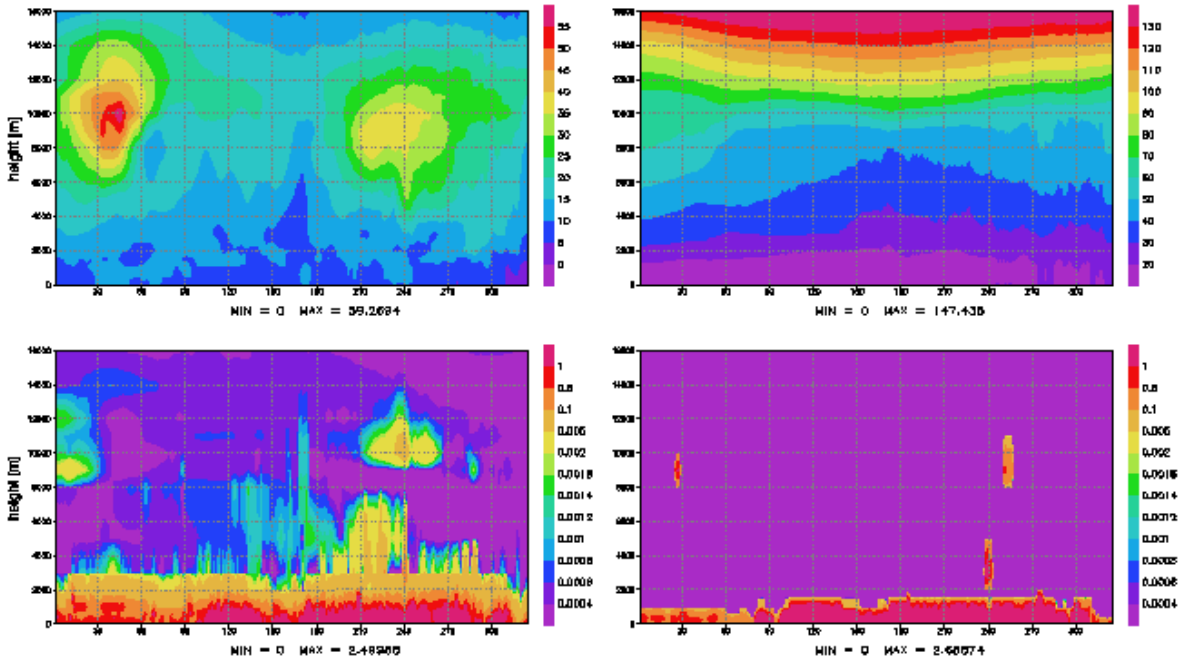

Figure 5: Vertical cross section from west to east along about 48 deg.N. (for 22 July 1999 00 UTC + 12 h). Top left: horizontal wind speed (m/s), new turbulence scheme. Top right: Potential temperature (C), new turbulence scheme. Bottom left: Turbulent kinetic energy (m^2/s^2), new turbulence scheme. Bottom right: Turbulent kinetic energy (m^2/s^2), old turbulence scheme.

damps the shear production of TKE significantly. Thus, the corresponding TKE maximum has a rather low magnitude and is shifted towards the region with weaker thermal stability to the west of the jet. Furthermore, above the mixed boundary layer, which has a height of about 1500 m, the new scheme generates a considerable entrainment zone. Also, deeper TKE outbreaks are simulated at some places. The sharp upper borders of the boundary layer in both versions are due to the coarse vertical model resolution in comparison with the strong vertical TKE-gradients in this regions.

The new TKE- and surface-layer schemes have been tested in a number of parallel experiments to tune the free empirical parameters and to compare with the operational forecasts using the old diagnostic schemes. As an example from these runs, Fig. 6 illustrates the performance of LM with the new turbulence package (using a pattern length of $L_{pat} = 500m$ and certain estimates of other parameters) versus the performance of the operational LM. The 2m temperature, the 2m dew point, the 10m wind speed and the 2m spread (2m temperature minus 2m dew point), predicted by the operational LM and by the new version of LM, exp_3306, are compared with the LM analysis. The curves show values of the weather elements averaged over a portion of the LM domain that is most densely covered with observations. Notice that the 2m temperature and the 2m dew point in the LM analysis come from the synoptic measurements. This is not the case for 10m wind that is a purely diagnostic quantity dependent on the interpolation procedure used in the surface-layer scheme. Therefore, the plots of 10m wind only indicate the difference between the various parameterizations.

As seen from the figure, the new version of LM shows a better overall agreement with observations. A marked difference in the diurnal variation of the 2m dew point between the two versions of LM should be emphasized. In the operational LM, the diurnal course of the 2m dew point is a slightly modified re-scaled replica of the diurnal course of the 2m temperature. This is related to the diagnosis of the 2m dew point through the assumption of height-constant relative humidity in

the surface layer. It leads to a strong underestimation of the dew point past 15h forecast time and, consequently, to an overestimation of the 2m spread. The latter quantity is of importance for the forecast of fogs. This overestimation is no longer the case with the new version of LM, where the diurnal course of the 2m dew point seems to be more physically realistic and compares better with observations.

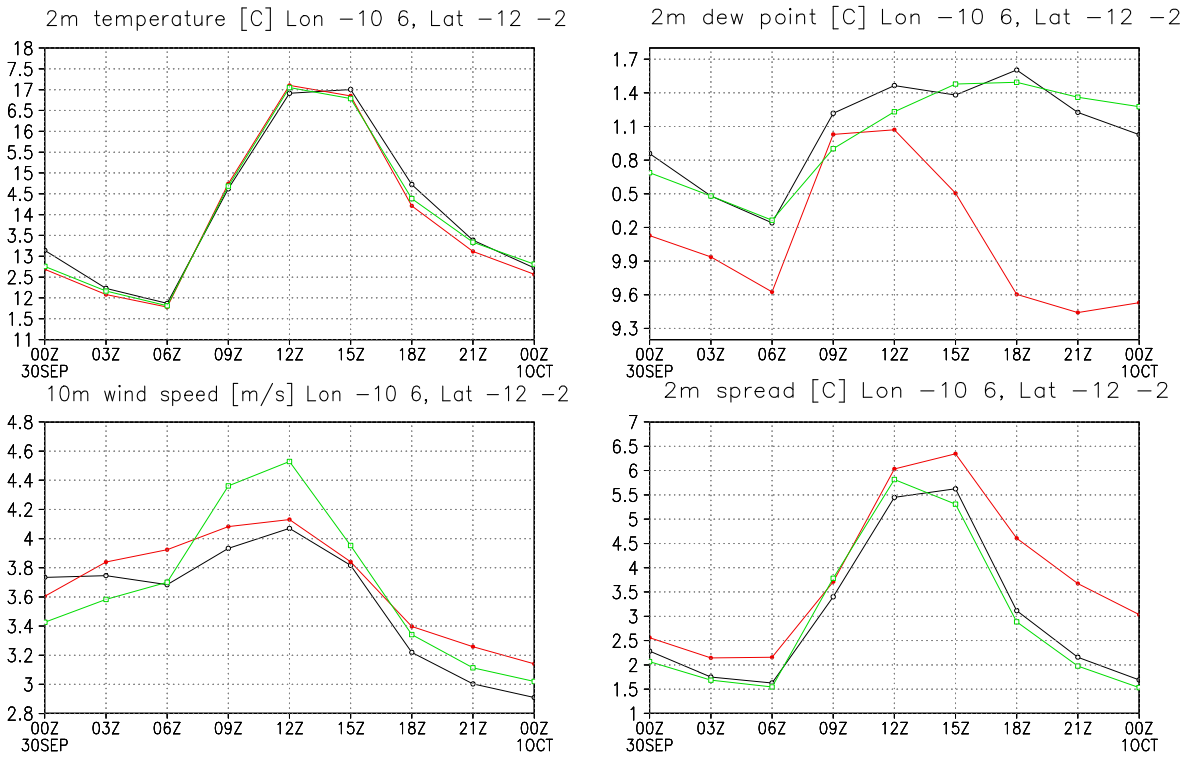

Figure 6: The 2m temperature, 2m dew point, 10m wind speed and 2m spread from the LM analysis (black curves with open circles), from the LM operational forecast (black curves with closed circles) and from a parallel experiment exp_3306 (grey curves). The time, UTC, and the date, 30 September 2000, are indicated at the x-axes.

A detailed statistical evaluation of the parallel runs with the new turbulence package (Raschendorfer and Mironov, 2001) revealed a number of improvements. The negative bias of 2m dew point temperature as well as the positive bias of 10m wind speed was found to be largely reduced. Also, higher 2m temperatures during the evening and the night hours are predicted on average, which have been known to be under-predicted by the old version. For operational forecasts at DWD, the new turbulence scheme has replaced the old scheme in May 2001.

6 Treatment of Grid-Scale Clouds and Precipitation

Cloud processes take place on scales that are significantly smaller than those resolved by the grid boxes of a NWP-model. In large-scale models not only cumulus clouds but also precipitating stratiform frontal clouds are of subgrid nature and need to be represented by a suitable prognostic cloud fraction parameterization (e.g. Sundqvist, 1988; Smith, 1990; Tiedtke,1993; Rasch and Kristjansson, 1998)). The formation of precipitation from subgrid stratiform clouds is further complicated by a necessary assumption on cloud overlap statistics (Jakob and Klein, 1999). This situation appears to be less complex in high-resolution mesoscale models with grid spacings of less than about 10 km. Frontal stratiform clouds are well resolved and bulk microphysical parameterizations

similar to those used in cloud resolving models (e.g. Kessler, 1969; Lin et al., 1983, Rutledge and Hobbs, 1983) may be applied. In these grid-scale schemes, only the cloud condensate is predicted by budget equations and the cloud cover is set to 100% whenever condensate occurs.

Except cumulus convection, which is parameterized by dedicated schemes, all other non-resolved clouds in mesoscale models are of stratocumulus-type. A direct hydrological impact of these clouds may be neglected for NWP purposes, but not the interaction with radiation. In LM, we use a traditional scheme that diagnoses a cloud fraction and a corresponding liquid water content in terms of relative humidity, pressure and convective activity. Clearly, subgrid-scale cloudiness will become less important with increasing model resolution.

Ice-phase processes play a significant role in mid-latitude frontal cloud systems and their impact should be taken into account by parameterization schemes. Two mechanisms of precipitation enhancement are of particular importance: the Bergeron-Findeisen process and the Seeder-Feeder mechanism, which both are based on the presence of supercooled liquid water. Nucleation of ice in a water saturated environment will cause a rapid growth of the ice crystals by deposition (because of the ice supersaturation) and riming (because of the presence of supercooled cloud droplets); the ice particle growth is at the expense of liquid water, but if the cloud is kept at water saturation by thermodynamic forcings, high precipitation rates may result from this Bergeron-Findeisen process. The Seeder-Feeder mechanism describes precipitation enhancement due to ice particles falling from a higher cloud into a lower cloud containing supercooled droplets; in this case, the droplets will also be converted into ice by deposition and riming, resulting in a more efficient removal of cloud water than by the collision-coalescence growth of water droplets.

Two gridscale cloud and precipitation schemes that include ice phase processes have been implemented in LM. They are described in the following sections and a shortcoming resulting from a simplified numerical treatment of precipitation fallout is also discussed. Both schemes neglect hail and graupel since these ice particle types are not relevant for precipitation formation in stratiform clouds at the current model resolution. The future application of LM on the mesoγ scale, however, will require a corresponding extension of the schemes.

6.1 The Operational Scheme

The default parameterization scheme for the formation of grid-scale clouds and precipitation is based on a Kessler-type bulk formulation and uses a specific grouping of various cloud and precipitation particles into broad categories of water substance. The particles in these categories interact by various microphysical processes which are parameterized in terms of the mixing ratios as the dependent model variables. Four categories of water substance are considered: water vapour, cloud water, rain and snow. Cloud water is treated a bulk phase with no appreciable terminal fall velocity relative to the airflow, whereas single-parameter exponential size-spectra and empirical size-dependent terminal fall velocities are assumed for raindrops and snow crystals.

To simplify the numerical solution of the budget equations for rain and snow, quasi-equilibrium in vertical columns is assumed by neglecting 3-d advective transport and by prescribing stationarity. The resulting balance between the divergence of the precipitation fluxes and the microphysical sources and sinks allows for a very efficient diagnostic calculation of P_r and P_s. While this assumption is well justified for large-scale models (Ghan and Easter, 1992), it is clearly not adequate for the meso-γ and smaller scales. Work on a prognostic treatment of the precipitation phases is in progress (see section 6.3). With these key assumptions, the equations for the hydrological cycle can be formulated as (see section 2.1 for symbols)

$$
\begin{aligned}
\frac{\partial T}{\partial t} &= A_T + \frac{L_V}{c_{pd}}\left(S_c - S_{ev}\right) + \frac{L_S}{c_{pd}} S_{dep} + \frac{L_F}{c_{pd}}\left(S_{nuc} + S_{rim} + S_{frz} - S_{melt}\right) \quad , \\
\frac{\partial q^v}{\partial t} &= A_{q^v} - S_c + S_{ev} - S_{dep}\,, \\
\frac{\partial q^c}{\partial t} &= A_{q^c} + S_c - S_{au} - S_{ac} - S_{nuc} - S_{rim} - S_{shed}\,, \\
\frac{1}{\rho\sqrt{G}}\frac{\partial P_r}{\partial \zeta} &= -S_{ev} + S_{au} + S_{ac} + S_{melt} - S_{frz} + S_{shed}\,, \\
\frac{1}{\rho\sqrt{G}}\frac{\partial P_s}{\partial \zeta} &= S_{nuc} + S_{rim} - S_{melt} + S_{frz} + S_{dep}\,.
\end{aligned}
\tag{27}
$$

The A_ψ-terms abbreviate advective and turbulent transport. L_V, L_S and L_F denote the latent heat of vapourization, sublimation and freezing, respectively. The following table describes the microphysical processes which are parameterized by corresponding mass transfer rates S_x.

Symbol	Definition / Description
S_c	Condensation and evaporation of cloud water.
S_{au}	Autoconversion of cloud water to form rain.
S_{ac}	Accretion of cloud water by rain.
S_{nuc}	Initial formation of snow due to nucleation from cloud water.
S_{rim}	Accretion of cloud water by snow (riming), $T < 273.16K$.
S_{shed}	Accretion of cloud water by snow to form rain (shedding), $T \geq 273.16K$.
S_{dep}	Depositional growth of snow.
S_{melt}	Melting of snow to form rain, $T > 273.16K$.
S_{frz}	Heterogeneous freezing of rain to form snow, $T < 267.16K$.
S_{ev}	Evaporation of rain in subcloud layers.

Both the Bergeron-Findeisen process and the Seeder-Feeder mechanism are represented explicitly by this scheme. The calculation of cloud water condensation and evaporation is based on instantaneous adjustment to water saturation. From the latter assumption, however, a number of major drawbacks result:

(a) Clouds will always exist at water saturation independent of temperature. That is, only mixed phase clouds – made up of cloud water, snow and rain – can be simulated below freezing point.

(b) The cloud ice-phase is neglected by assuming a fast transformation from cloud water to snow. Thus, the glaciation of clouds cannot be simulated and cirrus will be at a wrong thermodynamic state. Also, the precipitation enhancement from the Bergeron-Findeisen mechanism may be overestimated.

(c) High-level clouds usually exist at or close to ice saturation. Since the scheme requires water saturation for cloud formation, the initial conditions must be artificially adapted to avoid long spin-up periods: In the analysis scheme, the specific humidity obtained from measurements is increased by the ratio of the saturation vapour pressure over water and over ice for temperature below $0°C$. This affects the high-level humidity structure in an unphysical way.

To overcome these problems, a new scheme including cloud ice has been developed.

6.2 The LM Cloud-Ice Scheme

Many ice-phase schemes used in NWP-models solve only one prognostic equation for cloud condensate. Hence, the distinction of the water and the ice phase has to be determined diagnostically. This is done by (i) prescribing the liquid fraction in the total condensate as a function f_l of temperature and (ii) assuming that both ice and water are in thermodynamic equilibrium with respect to a hypothetical saturation vapour pressure given by $e_s = f_l\, e_s^w + (1 - f_l)\, e_s^i$, where e_s^w and e_v^i are the saturation vapour pressure over water and ice, respectively.

The function f_l for the liquid fraction is usually chosen to be 1 for $T > T_0 = 0°C$ and 0 for temperatures below a threshold T_{ice} with a linear or quadratic decrease with temperature in the range $T_{ice} < T < T_0$. Various values for T_{ice} are assumed in different schemes, ranging from -15 $°C$ to - 40 $°C$. Figure 7 shows an example for f_l used in the UKMO Unified Model together with some aircraft observations taken in frontal and non-frontal stratiform clouds. The observational data show low liquid fractions below about - 15 $°C$. A climatology shown by Feigelson (1978), however, suggests that there is plenty of supercooled water in the range - 15 to - 30 $°C$.

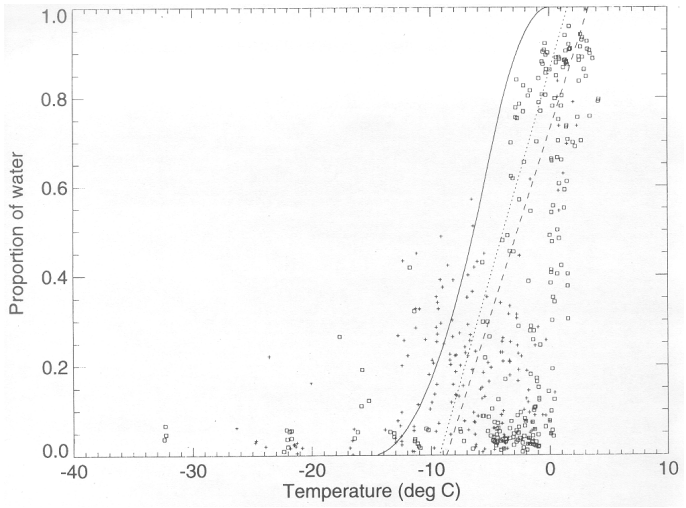

Figure 7: Liquid fraction from aircraft observations against temperature, as described by Bower et al. (1996). Crosses indicate clouds in continental clouds and squares indicate clouds in maritime clouds. The solid curve represents a parameterization used in the UKMO Unified Model. A similar parameterization is used in the ECMWF Model but with a threshold temperature of $-25°C$. The dotted lined is the best fit to the data for continental clouds and the dashed line for maritime clouds. Reproduced from Ryan (1996).

Ice-schemes with a prescribed liquid fraction are widely in use but have a number of conceptional drawbacks. First, the assumption of thermodynamic equilibrium of both water and ice at temperatures below T_0 is not in accordance with physical principles. Second, for $T < T_{ice}$ a saturation adjustment is done for the calculation of condensate; since the number of cloud ice crystals is very small, such an instantaneous adjustment has no physical basis. Third, effects from the Bergeron-Findeisen process cannot be considered explicitly, since the ice-phase is in thermodynamic equilibrium. Fourth, the Seeder-Feeder mechanism is not represented: deep clouds are more likely to be glaciated than thin clouds at the same temperature (Ryan, 1996). Also, ice falling from above into sub-freezing layers is forced to melt in order to maintain the prescribed liquid fraction. This is not very realistic.

Bearing in mind these difficulties, the new LM parameterization scheme was designed to take into account cloud ice by a separate prognostic budget equation. Cloud ice is assumed to be in the form of small hexagonal plates that are suspended in the air and have no appreciable fall velocity. As a

novel feature of the scheme, we formulate the depositional growth of cloud ice as a non-equilibrium process and require, at all temperatures, saturation with respect to water for cloud liquid water to exist. Ice crystals which are nucleated in a water saturated environment will then grow very quickly by deposition at the expense of cloud droplets. Depending on local dynamic conditions, the cloud water will either evaporate completely, or will be resupplied by condensation. For strong dynamical forcings it is expected that water saturation will be maintained, resulting in a mixed phase cloud. In case of a comparatively weak forcing, the cloud will rapidly glaciate to become an ice cloud existing at or near ice saturation (i.e. at subsaturation with respect to water). Figure 8 gives an overview on the hydrological cycle and the microphysical processes considered by the scheme.

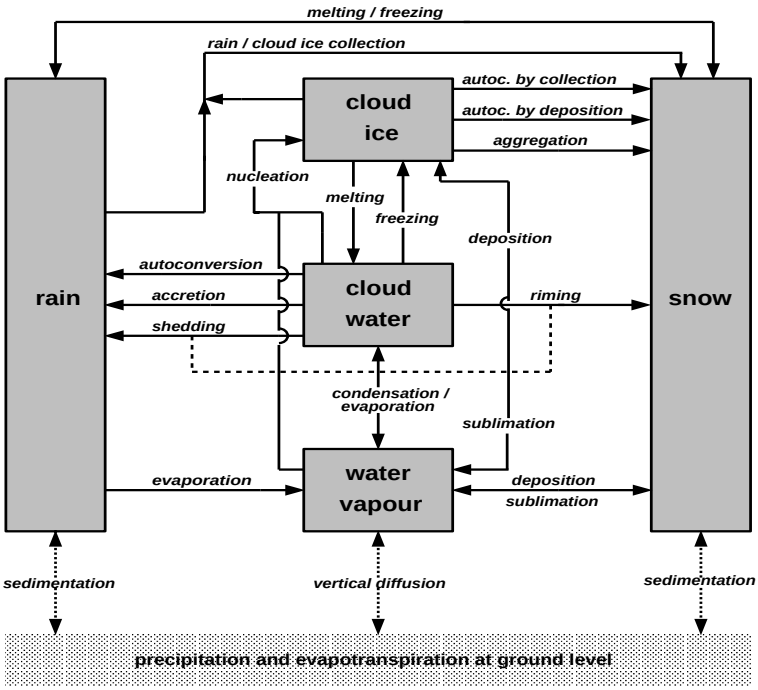

Figure 8: Hydrological cycle and microphysical processes in the LM cloud ice scheme

The explicit calculation of cloud ice depositional growth as a non-equilibrium process is based on the mass-growth equation of a single pristine crystal and requires assumptions on the shape, size and number density of the ice crystals:

- We assume a monodispers size distribution for cloud ice particles with the mean crystal mass

$$m_i \;=\; \rho q^i N_i^{-1}\,, \tag{28}$$

being diagnosed from the the predicted mixing ratio q^i and the number density N_i of cloud ice particles.

- The number density $N_i(T)$ of cloud-ice particles is prescribed as a function of ambient air temperature using the relation

$$N_i(T) \;=\; N_0^i \exp\{\,0.2\,(T_0 - T)\}\,, \qquad N_0^i \;=\; 1.0 \cdot 10^2 m^{-3}\,, \tag{29}$$

which is an empirical fit to data obtained by aircraft measurements in stratiform clouds (Hobbs and Rangno, 1985, and Meyers et al., 1992). For a given temperature, the experimental data may scatter by about two orders of magnitude. Nevertheless, we assume that

(29) represents a meaningful average value for the cloud ice crystal concentration in cold stratiform clouds.

- Cloud ice crystals are assumed to be in the form of thin hexagonal plates with diameter D_i and thickness h_i, where the maximum linear dimension D_i is smaller than about 200 μm. This constant aspect ratio growth regime yields the following relation to calculate the size D_i of cloud ice particles from the diagnosed mean mass m_i,

$$D_i \;=\; (m_i)^{1/3}\,(a_m^i)^{-1/3}\,, \tag{30}$$

where $a_m^i = 130$ kgm^{-3}. A temperature dependency of the form factor a_m^i is neglected.

Using (28), (29) and (30) in the mass-growth equation for a single crystal, the total deposition rate of cloud ice, $S_{dep}^i = N_i \dot{m}_i/\rho$, may then be formulated by

$$S_{dep}^i \;=\; c_i\, N_i\, m_i^{1/3}\,(q^v - q_{si}^v) \tag{31}$$

in terms of ice supersaturation (or subsaturation for sublimation). q_{si}^v is the specific humidity at ice saturation. The factor $c_i = 4G_i d_v \sqrt[3]{a_m}$ varies slowly with temperature and pressure due to the Howell factor G_i and the diffusivity d_v of water vapour. Here, c_i is approximated by the constant value of $1.5 \cdot 10^{-5}$.

Cloud ice is initially formed by heterogeneous nucleation or homogeneous freezing of supercooled droplets. The latter process is parameterized by instantaneous freezing of cloud water for temperatures below $-37°C$. To formulate heterogeneous nucleation, we simply assume that the number of ice forming nuclei activated within a time step Δt is given by Eq. (29) and that the temperature is below a nucleation threshold (set to $-7°C$). We will also neglect nucleation whenever ice is already present since this has been found to be of minor importance. Recent field experiments show that ice nucleation is not likely to occur in regions of the atmosphere which are subsaturated with respect to water, except for very low temperatures. In the present version of the scheme we thus require water saturation for the onset of cloud ice formation above a temperature threshold T_d (set to $-30°C$). For temperatures below T_d, deposition nucleation may occur for ice supersaturation. All other conversion rates are parameterized in a similar way as in the operational scheme. For 3-dimensional advection of cloud ice, the positive definite Lin and Rood (1996) algorithm is used.

The LM cloud ice scheme has been tested for a number of case studies. Figure 9 shows the variation with temperature of the liquid fraction $f_l = q^c/(q^c + q^i)$ generated by the scheme. The values of f_l were obtained from a single time step after the model was run for 12 h starting from the 4 May 2001 00 UTC analysis. For temperatures warmer than about $-10°C$, there are cloudy grid-boxes which are composed of either liquid water or ice, and there is a large number of boxes indicating a mixed phase. Below $-10°C$, there is still a large number of mixed phase clouds with supercooled droplets, but the liquid fraction drops off with temperature. Below about $-35°C$ only ice clouds exist. There is a good qualitative agreement with the observations for stratiform clouds in Figure 7, but the model indicates a larger number of mixed phase clouds for temperatures below about $-15°C$. In Figure 9, however, not only stratiform clouds but all cloudy grid points are counted. For the convective 4 May 2001 case, a large number of gridpoints from anvils and embedded cold frontal convection contribute to the scatter plot. At such points, strong dynamical forcing can keep the air at water saturation allowing for mixed phase clouds at low temperatures. This example shows that with the new scheme the liquid fraction adjusts reasonable in response to dynamical forcing and microphysical processes.

There is also a large impact to the humidity structure of the upper atmosphere. To illustrate this, the relative humidity over ice obtained from runs with the cloud ice and the operational scheme

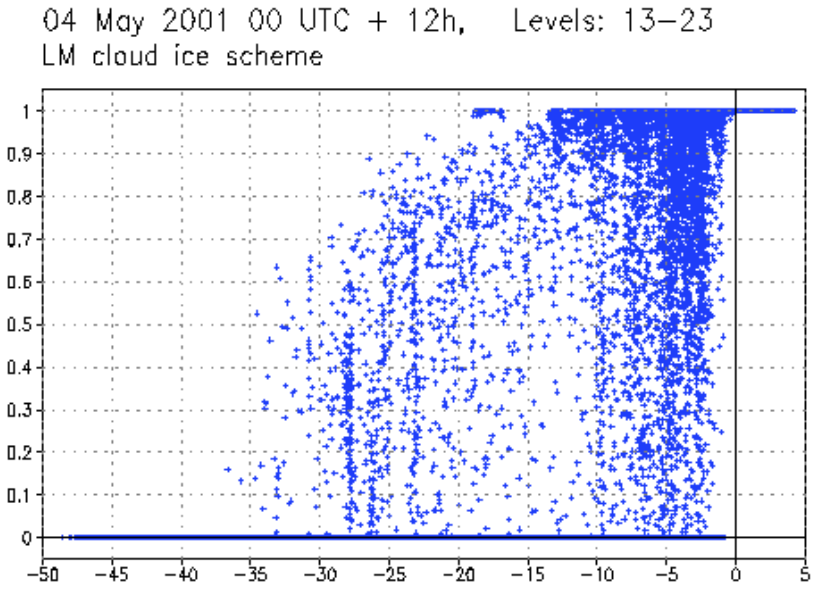

Figure 9: Variation with temperature of the liquid fraction for 4 May 2001 00 UTC + 12 h.

is shown in Figure 10 for the same case and forecast time. Figure 11 displays the corresponding specific cloud ice and cloud water contents. The fields are plotted for a model subdomain at level 14, corresponding to a height of about 7000 m with temperatures ranging from -30 to $-40°C$. The operational run reveals high ice supersaturation of about 20 - 40 % in two regions: a band-like structure over western France which is associated with a cold front, and a more unstructured region in the warm sector ahead of the front. Here, widespread deep convection occurs which by vertical transport generates and maintains high humidity. With the operational scheme, there is no ice but only cloud water by definition (Fig. 11, right). Since saturation with respect to water is required for grid-scale cloud formation, cloud water is found only at those gridpoints where dynamic forcing by convection drives the atmosphere to water saturation (at a temperature of $-35°C$, this will occur at about 35 % ice-supersaturation). However, these points are rather scattered whereas satellite images indicate a region of merged anvils above the northern Mediterranean Sea and southern France (not shown). This high level cloudiness is simulated much more realistic by the cloud ice scheme (Figures 10 and 11, left). Here, cloud ice is initially formed also at gridpoints which are at or near water saturation. Subsequently, however, it can be advected into regions which are ice-supersaturated but are below water saturation. In these regions, cloud ice will continue to grow by vapour deposition, thereby reducing the humidity to values more close to ice saturation (Fig. 10, left). Thus, a much larger region with grid-scale anvils – mostly composed of ice – is simulated than with the operational scheme. In the warm sector region, some mixed-phase clouds do also exist at gridpoints, where strong convective forcing maintains water saturation. Also, high-level ice clouds appear along cloud front.

For the test cases considered so far, there was no remarkable impact to the predicted precipitation. The total precipitation amount can increase or decrease by about 10 %, depending on the weather situation. The main advantage of the scheme is a more physically based representation of ice and mixed-phase clouds, allowing for a direct simulation of cloud glaciation. The phase composition of high-level clouds appears to be well captured, which is important for a better cloud-radiation interaction. And in particular, the formation, growth and spreading of grid-scale anvil clouds can be simulated explicitly. Following further testing it is planned to introduce the cloud ice scheme operationally in spring 2002. To provide consistent boundary conditions from the driving model,

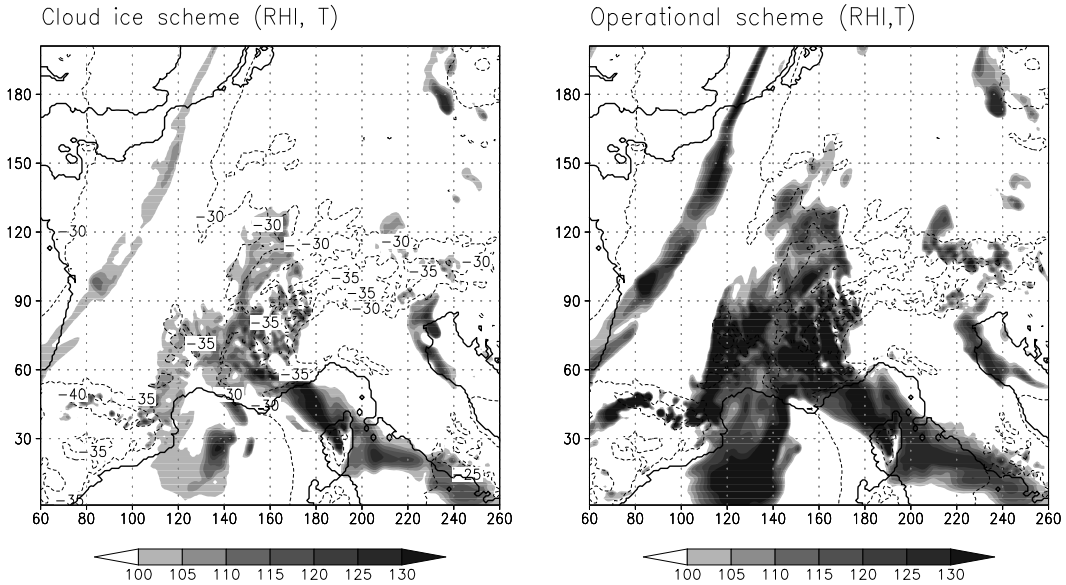

Figure 10: Relative humidity over ice (shaded, in %) and temperature ($°C$, isolines) for 4 May 2001 00 UTC + 12 h at model level 14. Left: cloud ice scheme. Right: operational scheme.

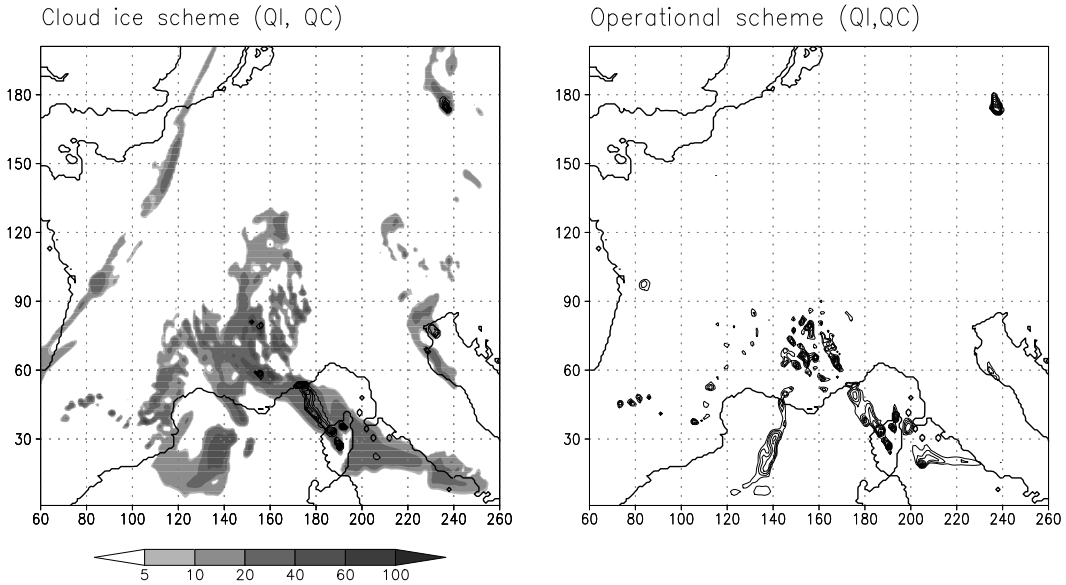

Figure 11: Specific cloud ice content (shaded, in mg/kg) and cloud water content (isolines at 10 mg/kg intervals) for 4 May 2001 00 UTC + 12 h at model level 14. Left: cloud ice scheme. Right: operational scheme.

the scheme has also been implemented in our global model GME. A rerun of a one-year period during 2000/2001 revealed an overall beneficial impact of the cloud ice scheme, with a significant reduction of current imbalances in the average energy and water budgets.

6.3 Full 3-D Transport of Precipitation

The operational scheme for gridscale precipitation assumes column equilibrium for precipitating constituents rain and snow. That is, sedimentation can be considered to be a fast process compared to the characteristic time scale of advection. By increasing the model's spatial resolution, this

assumption gets more and more unrealistic. With the characteristic values of 5 m/s for the terminal velocity speed of rain and of 1 m/s for snow, the time scales for sedimentation of rain and snow are estimated as 500 s and 2500 s, respectively, by assuming a vertical fall distance of typically 2500 m for frontal precipitation. At 15 m/s wind speed, the corresponding horizontal displacements are about 8 km for rain and 40 km for snow – an effect should be taken into account for grid spacings of 10 km or smaller. Horizontal transport is particularly important for the generation of lee-side precipitation, which is not sufficiently recognized by the operational LM. When going to the meso-γ scale, deep convection becomes resolved explicitly. Here, all instationary effects of cloud development, and especially the vertical advection of the precipitation phases must be considered to simulate realistically the life-cycle of deep convective cells.

In order to take these effects into account, the diagnostic equations for the precipitation fluxes P_x from the equation set (27), where x stands for r (rain) or s (snow), respectively, have to be replaced by full prognostic equations for the mixing ratios q^x:

$$\frac{\partial q^x}{\partial t} + \mathbf{v} \cdot \nabla q^x - \frac{1}{\rho}\frac{\partial}{\partial z}(\rho v_x^T q^x) = S_x \,. \tag{32}$$

Here, v_x^T denotes the terminal fall velocity, which is a nonlinear function of q^x. The transformation of the parameterization scheme (27) into a 'prognostic scheme' using (32) requires three steps: (i) a reformulation of the microphysical processes S_x in terms of q^x as dependent model variables, (ii) an accurate and positive definite advection scheme, and (iii) a numerically efficient treatment of the sedimentation term.

Since the precipitation fluxes and the mixing ratios are uniquely related by basic parameterization assumptions, the reformulation of the source terms is straightforward. For threedimensional advection, the Lin and Rood (1996) algorithm is used. The numerical treatment of sedimentation turns out to be more difficult: in case of precipitation falling through thin model layers near the surface, the Courant number may become larger than one. An implicit scheme, however, cannot be applied because the sedimentation velocity is a nonlinear function of the mixing ratio. Also, a semi-Lagrangian technique will be difficult to apply since the source terms have to be taken into account to allow for microphysical interactions during fallout. For the current testversion of the prognostic scheme, we have developed (Gassmann, 2001) a relatively efficient integration method for (32). It is based on symmetric Strang process-splitting combined with local time-splitting for the sedimentation process (i.e. only for those layers where the local Courant number exceeds the stability limit).

A number of test cases have been run with the prognostic scheme to investigate the impact of rain and snow advection at the current 7 km grid spacing of LM. One case considered the Brig flash flood in September 1993 which caused a lot of damage in the city of Brig near the eastern end of the upper Rhone Valley. Figure 12 (left) shows the observed precipitation for a model subdomain covering the southwestern part of the Alps. Strong southerly flow causes an enormous precipitation amount along the southern ridge of the the Alps, but also the lee region north of the ridge and especially the upper Rhone Valley is affected. With the operational model version (Fig. 12, right), most of the precipitation is confined to the southern ridge and only relatively little rain penetrates to the lee side. The Rhone Valley is almost dry and at the Brig gridpoint there is no precipitation at all. The precipitation forecast improves remarkably by using the prognostic scheme (Fig. 12, middle). Here, horizontal transport with the southerly flow results in a much larger precipitation amount north of the ridge, particularly for the upper Rhone Valley. Also, the region of maximum precipitation shifts northeast and is thus more close to the observations. In particular, the precipitation field is much smoother with a significant reduction of the maximum

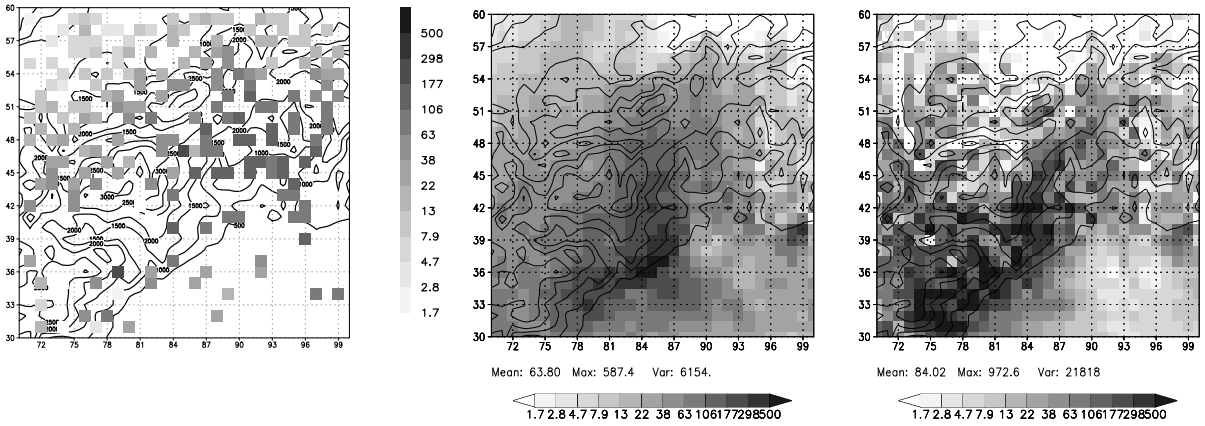

Figure 12: 24-h accumulated precipitation for the Brig case, 23 September 1993 6 UTC – 24 September 1993 6 UTC. Left: Observations; middle: LM-simulation using the prognostic precipitation scheme; right: LM-simulation using the operational precipitation scheme. The (x,y) gridpoint indices of Brig are (83,48).

value and the variance. However, the area mean value decreases by about 25%.

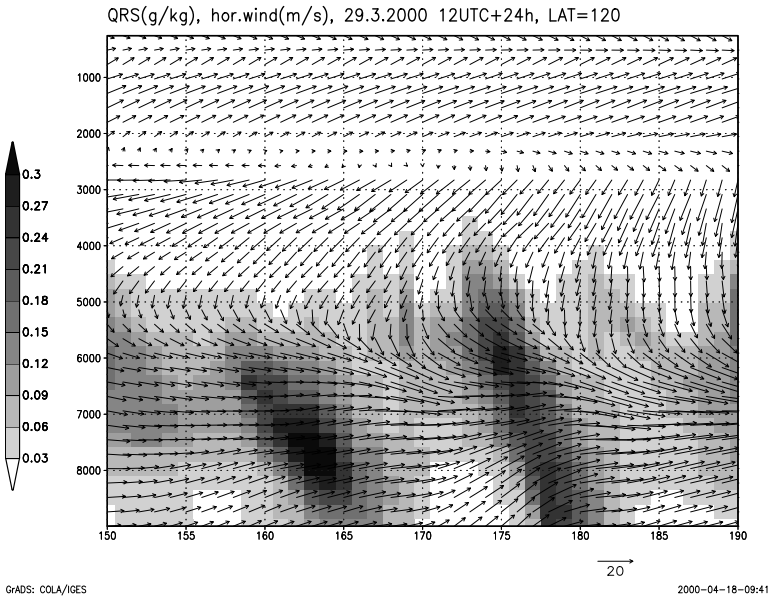

Figure 13: Vertical west–east cross section over the Rhine valley near Freiburg for 29 March 2000 12 UTC + 24 h. Shaded: mixing ratio of rain and snow; arrows: horizontal wind, indicating a westerly flow in the lower atmosphere. The vertical spacing is on model levels. The Rhine valley is located at gridpoints 171-176, with the Vosges to the left and the Black Forest to the right.

We suggest two physical reasons to be responsible for the reduction of area mean precipitation in mountainous regions by using the prognostic scheme. To illustrate this, Figure 13 shows a vertical cross section of the mixing ratio of rain and snow over the Rhine Valley near Freiburg for another case. Obviously, rain and snow are generated by orographic lifting over the Vosges and the Black Forest in near-surface westerly flow. Advection of the mixing ratio q^x then results in a large horizontal displacement before precipitation reaches the surface (is this case by about 5 gridpoints corresponding to 35 km). Consequently, a larger spatial area is available for sub-cloud evaporation

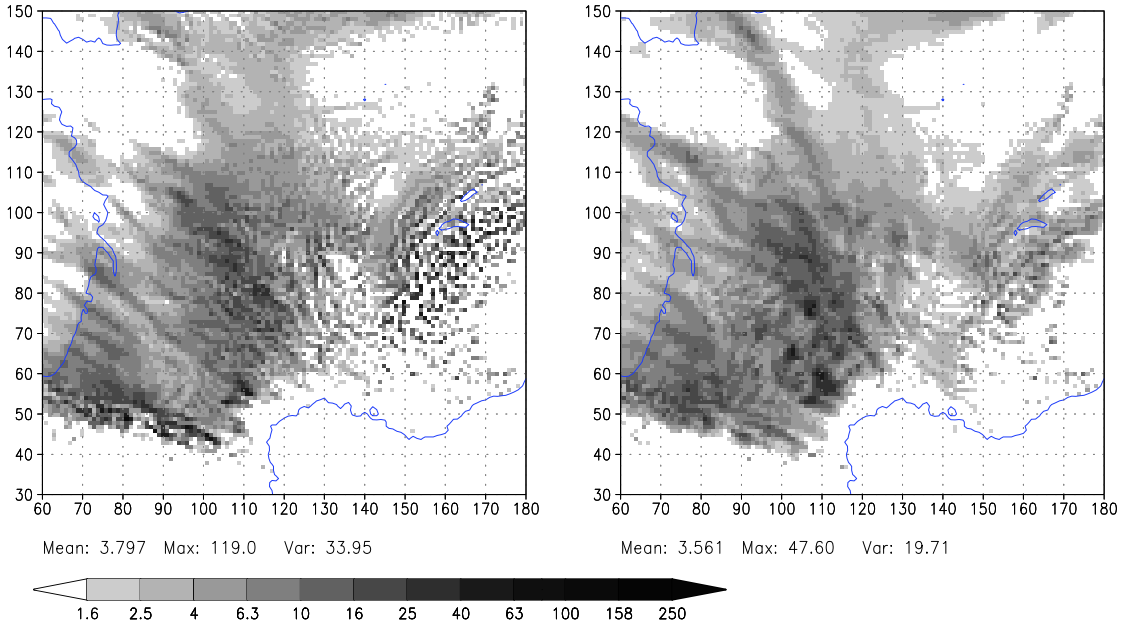

Figure 14: 12-hr accumulated precipitation (mm) from an LM-simulation of 2 February 2000 06 - 18 UTC. Left: reference version. Right: experimental version with the prognostic precipitation scheme.

(particularly in the dry lee-side region) than in the diagnostic scheme. Another reason contributing to the reduction of precipitation amount is a weakening of the seeder-feeder mechanism: In contrast to the prognostic scheme, all snow crystals must fall through the same vertical column where they are generated aloft when using the diagnostic scheme. This certainly gives the maximum effect of precipitation enhancement due to the seeder-feeder process.

The prognostic treatment of the rain and snow mixing rations has also a beneficial impact in non-mountainous regions. Figure 14 shows the 12-h accumulated precipitation amount for a case with a cold front crossing France from northwest. Compared to the operational run the predicted precipitation field appears much less heterogeneous, with reduced spatial variability not only over the Alps and the Pyrenees, but also for the mid-range mountain systems and the more flat regions in western France. These first case studies show overall encouraging results for the prognostic scheme, and a number of shortcomings of the operational version seem to be overcome. For an operational application of the scheme, a detailed statistical evaluation as well as some numerical optimization remain to be done.

7 Representation of Moist Convection at High Spatial Resolution

The parameterization of convection poses serious problems in numerical models of the atmosphere, and in fact convection seems to be an ill-posed parameterization problem. Parameterizations have to rely on the assumption of a statistical equilibrium between the resolved scales and the parameterized scales. This requires at least a spectral gap between resolved and parameterized processes. Typical space and time scales of convection are in the order of 10 km and 1h, respectively. The horizontal resolution of NWP-models for the meso-β scale is of the same order and the time step is of the order 1 min. Neither in the horizontal scale nor in the time scale a gap exists between resolved

scales and convection. Nevertheless, experience shows that a parameterization of deep convection is necessary in models of the aforementioned resolution.

At present, the Tiedtke (1989) mass-flux scheme is used (with only minor changes) to parameterize convection in the LM. Originally, the scheme has been designed for large-scale models. Experiences from the operational application reveal, however, that no severe problems result from applying the scheme (i) on the meso-β scale at a grid spacing of only 7 km, and (ii) within a nonhydrostatic framework. Also, the scheme is CISKable because of its Kuo-type closure (see below), but no grid-point storm like effects have been noticed so far. Convection associated with relatively strong synoptical forcing, e.g. along cold fronts, is in general well represented. Deficiencies occur in case of air-mass thunderstorms with weak large-scale forcing: the diurnal cycle is not well captured (the convective activity peaks at noon) and the location is often not correct. Mesoscale organization of convection cells is also a problem (squall-line formation is often miss-placed or too weak) and deficiencies in case of orographical forcings may be present. Problems of this type may arise partly from the ill-posedness of the parameterization problem and partly from shortcomings of the scheme itself. In this section we try to address a few of these aspects.

7.1 Parameterization by Mass-Flux Schemes

Most mesoscale models use mass-flux schemes to represent deep and shallow moist convection. In contrast to adjustment schemes or the well known Kuo scheme (Kuo, 1974), these schemes are based on a more elaborated physical model of how a subgrid-scale convective circulation affects the resolved scales by latent heat release and by vertically redistributing heat, moisture and momentum. Basically, any mass-flux scheme is made up of three main components: feedback, redistribution and closure.

- *Feedback*
  The calculation of the time-tendency of resolved variables due to subgrid-scale convective fluxes (i.e. the feedback) is based on the generic budget equation for a prognostic variable ψ $(= \theta, q_v, u, v)$ averaged over a model grid volume,

$$\frac{\partial \psi}{\partial t} + \frac{1}{\rho}\nabla \cdot (\rho \mathbf{v} \psi) = -\frac{1}{\rho}\frac{\partial}{\partial z}(\rho \overline{w'\psi'}) + \overline{S}_\psi \,, \tag{33}$$

  where the overbar indicating a gridbox mean has been omitted on the lefthand side. S_ψ is the body source term of ψ and other symbols have their usual meaning. In order to derive a tractable formulation for the convective fluxes $\overline{w'\psi'}$, it is assumed that the area of a gridbox may be decomposed into a fraction σ_u with convective updrafts, a fraction σ_d with convective downdrafts and an environmental fraction $\sigma_e = 1 - \sigma_u - \sigma_d$, such that the average value of ψ may be formulated as

$$\overline{\psi} = \sigma_u \psi_u + \sigma_d \psi_d + (1 - \sigma_u - \sigma_d)\psi_e \,,$$

  with ψ_u, ψ_d and ψ_e being mean values over the corresponding area fractions. A similar decomposition is done for the source term S_ψ. By the additional assumptions that the area fraction of both updrafts and downdrafts is very small and that the environmental values ψ_e may be approximated by the grid-volume means, the convective fluxes can be formulated as

$$\rho \overline{w'\psi'} = M_u(\psi_u - \psi) + M_d(\psi_d - \psi) \,, \tag{34}$$

  where $M_{u,d} = \rho \sigma_{u,d} w_{u,d}$ denotes the total updraft and downdraft mass flux, respectively.

- *Redistribution*
  When reintroducing (34) into (33) it is still necessary to calculate the vertical redistribution of the dependent variables due to updraft and downdraft transports. This is usually done by using a simple steady state plume model for the cumulus elements. Examples of such models are given by Yanai et al. (1973), Tiedtke (1989), and others. They may be sketched as

$$\frac{\partial M_u}{\partial z} = E_u - D_u \tag{35}$$

$$\frac{\partial M_u \psi_u}{\partial z} = E_u \psi - D_u \psi_u + S_u \tag{36}$$

  for the updraft and analogously for the downdraft. The entrainment and detrainment rates must be specified. The cloud model determines the vertical structure of both the mass-fluxes and the in-cloud variables and thus the vertical profile of the feedback. Note that the vertical variation of the mass-flux M_u is entirely determined by the entrainment/detrainment rates.

- *Closure*
  In order to integrate the cloud model equations (35) and (36) numerically, it is finally required to specify the updraft mass-flux M_b at cloud base in terms of the resolved variables. Of course, a boundary condition for the mass-flux M_t at the top of the downdrafts is also needed. But usually a simple linear relation between M_t and M_b is assumed, resulting in a closure condition for M_b only. Whereas the cloud model equations determine the vertical structure of the feedback, the specification of M_b determines the magnitude of the heat and moisture release. In this way the closure condition is of crucial importance in any mass-flux scheme. Several different methods have been proposed for convective closure. They may be broadly classified into equilibrium types and non-equilibrium types.

  (i) Equilibrium closure
  These closures postulate a statistical equilibrium between the sub-grid scale convection and the resolved flow. An example is the Arakawa-Schubert (1974) scheme, where the closure is based on an equilibrium assumption for convective available buoyant energy (CAPE),

$$E_{cp} = \int_{z_b}^{z_t} \frac{g}{\theta_v}(\theta_{v,u} - \theta_v) dz \,. \tag{37}$$

  z_b and z_t denote the cloud base and cloud top, respectively. By assuming that convection consumes CAPE at the same rate as it is supplied by large-scale forcing - thus implying E_{cp} to be constant with time – an equation for M_b may then be derived. Another example is the Kuo-type closure used in the Tiedtke-scheme. Here, a statistical equilibrium is assumed for the sub-cloud moisture content,

$$\frac{\partial}{\partial t} \int_{z_s}^{z_b} \rho q_v dz = 0 \,, \tag{38}$$

  such that the subcloud specific humidity is consumed by convection at the same rate as it is supplied by large-scale moisture convergence (z_s is the height of the surface).

  (ii) Non-equilibrium closure
  Whereas in case of an equilibrium closure no large deviations from the postulated equilibrium may arise, there is no explicit control on the feedback when a non-equilibrium closure is applied. This does not mean that with these types of schemes the feedback will not come in equilibrium with the dynamical forcing. The adjustment to equilibrium, however, will not be instantaneous. The Fritsch and Chappel (1980) scheme provides an example of an adjustment type non-equilibrium closure, where the cloud-base mass flux is calculated from the condition that the CAPE is consumed over a convective time scale τ:

$$\frac{\partial E_{cp}}{\partial t} = -\frac{E_{cp}}{\tau} \tag{39}$$

Another example is a closure used in the UKMO Unified Model, where the cloud base mass-flux is set proportional to the initial buoyancy B_c of an air parcel when lifted over the pressure interval Δp_c of one model layer above cloud base: (Gregory and Rowntree, 1990):

$$M_b = c \cdot B_c / \Delta p_c \tag{40}$$

7.2 Sensitivity to Closure Assumptions

In the operational LM, the Kuo-type closure (38) is applied, as in the original Tiedtke-scheme. Using the budget equation (33) for specific humidity q_v and the requirement that the subcloud moisture content is constant in time, the closure for the cloud-base mass-flux in principle reads

$$M_b = -\frac{1}{q_{v,u} - q_v} \int_{z_s}^{z_b} \left(\rho \mathbf{v} \cdot \nabla q_v + \frac{\partial F^{q_v}}{\partial z} \right) dz \quad , \tag{41}$$

where the turbulent vertical flux F^{q_v} of specific humidity has also been included in the calculation of the moisture convergence.

In order to get an idea on how sensitive the mass-flux scheme is to the closure condition, two alternative non-equilibrium closures were tested. The first is a CAPE-based condition, but instead of using the relaxation condition (39) towards an equilibrium state a more direct approach is proposed: Since CAPE measures the upper limit of the potential energy which can be transformed to kinetic energy of vertical motion, $\sqrt{E_{cp}}$ is an upper estimate for the mean in-cloud vertical velocity. This suggests a closure condition in the form

$$M_b = C_{cp} \rho_{z_b} \sqrt{E_{cp}} \,, \tag{42}$$

which is similar to (40), but takes the complete potential instability in a vertical column into account. C_{cp} is a dimensionless tuning parameter.

The second non-equilibrium closure is based on turbulent kinetic energy (q^2), being predicted by the new LM turbulence scheme. In conditionally unstable situations the vertical average of q^2 over cloud depth,

$$E_{tke} = \frac{1}{z_{top} - z_b} \int_{z_b}^{z_{top}} q^2 dz \tag{43}$$

is used in the closure condition for the cloud base mass-flux. A relation in the form

$$M_b = C_{tke} \frac{\rho}{g} E_{tke} \quad , \tag{44}$$

is suggested, where C_{tke} is an inverse time constant, acting as a tuning parameter. The rationale for this closure method is the close connection between the convective available energy and the buoyant production term in the prognostic equation for turbulent kinetic energy. If this term is positive and large, there will also be a considerable amount of convective available energy, as the difference between the updraft temperature and the environmental temperature will be large. Therefore, large values of convective available energy are connected to a large buoyant production of TKE. If this term dominates the tendency of TKE, a growth of TKE is possible, postponing the time of the maximum convective activity.

For all three closure conditions a maximum value for the cloud base mass flux of $1 kg/(m^2 s)$ is prescribed. No additional parameter is required for the Kuo-type closure. For the two non-equilibrium closures minimum values of $E_{cp} = 1 m^2/s^2$ and $E_{tke} = 0.05 m^2/s^2$, respectively, are prescribed which have to be exceeded to allow for the onset of convection. The tuning parameters are set to $C_{cp} = 0.01$ and $C_{tke} = 10 s^{-1}$ by default.

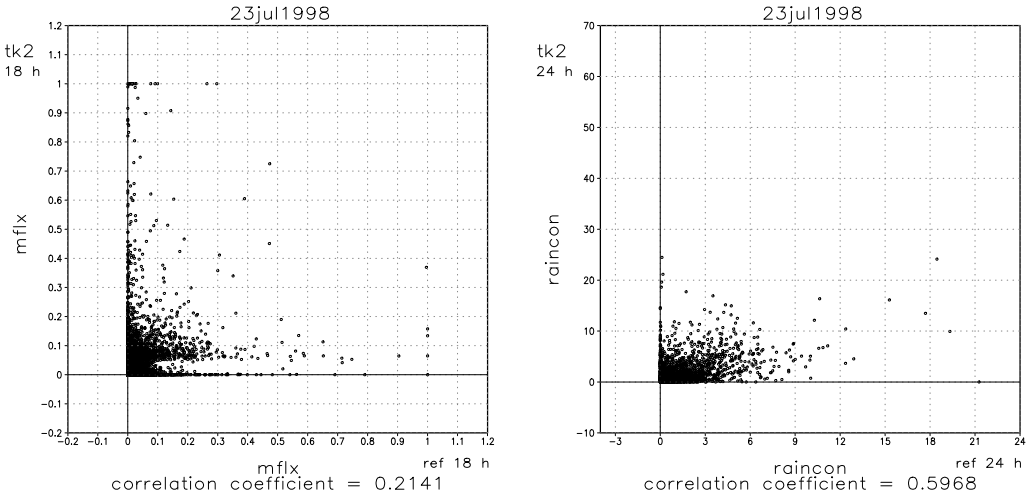

Figure 15: Left: Scatter-plot of the cloud-base mass flux from a model run using the TKE-closure versus the mass flux from the reference run using the Kuo-type equilibrium closure for 23 July 1998 00 UTC + 18h. Right: As in the left picture, but for the accumulated convective precipitation in the time period 18-24h.

A preliminary test experiment to compare the three closure conditions has been performed by 24 hour forecasts starting on 23 July 1998 00 UTC on the full domain of the operational LM. This case is a typical summertime convective situation with weak synoptical forcing and heavy thunderstorms developing in the late afternoon. The left scatter plot in Figure 15 shows the cloud base mass-flux (in $kg/(m^2 s)$) from the run with TKE-closure (44) versus the mass-flux from the reference run using the closure (41) based on moisture convergence after 18 hours of simulation time. The results reveal very low correlation between the two closure conditions. Looking at the convective rain amount in the subsequent 6h period, of course part of this difference is smoothed out. But still the correlation is rather low (Fig. 15, right). A very similar result is obtained by using the CAPE-closure (42).

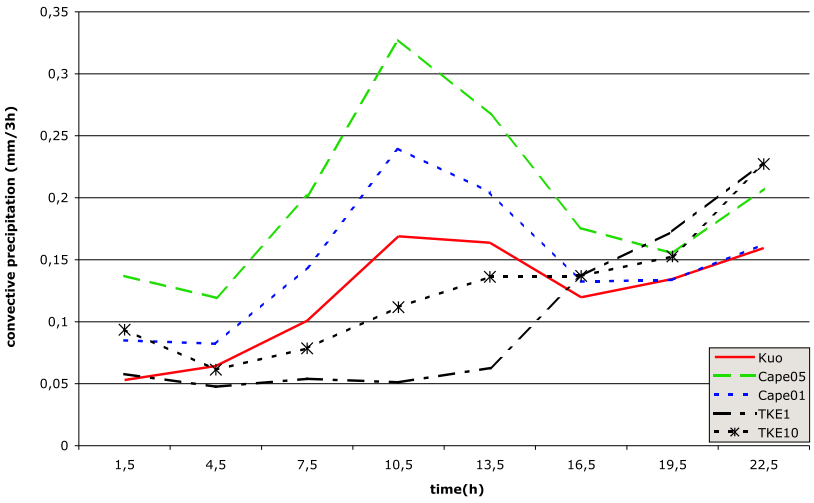

Figure 16: Left: Area-average of convective precipitation for 23 July 1998 00 UTC as function of forecast time (see text), using various variants of mass-flux closure.

The time series of total-domain area-averaged convective rain in Figure 16, where the Kuo, Cape01 and TKE10 runs used the tuning parameters as given above, shows for Kuo and Cape01 the well known tendency of parameterized convection to peak around local noon. This tendency is clearly reduced by the closure using the vertical mean of turbulent kinetic energy. However, it must be kept in mind that the values of the tuning parameters greatly influence the parameterized convective precipitation. Using $C_{cp} = 0.05$ (Cape05) and $C_{tke} = 1.0s^{-1}$ (TKE1), respectively, shows a more or less parallel shift of the cape results. In contrast, the lower value of the tuning parameter for the TKE-closure nearly cancels all convective activity before noon. By this, a large amount of convective instability seems to have remained, becoming liberated during the afternoon hours. A similar effect occurs if the minimum values of E_{cp} and E_{tke}, respectively, are increased (not shown).

7.3 Open Questions and Possible Improvements

The application of traditional mass-flux convection schemes in nonhydrostatic models for the meso-β scale poses a large number of open questions and only a few can be discussed here. The results from the preceding section reveal a large impact of the type of the closure method: By adjusting free parameters in two versions of non-equilibrium closure conditions, the diurnal cycle of summertime convection could be simulated much more realistic than using an equilibrium closure based on moisture convergence, and also the total precipitation amount was found very sensitive. This is in contrast to large-scale modelling, where Gregory (1995) found only a relatively small impact from using various closure methods. Thus, an appropriate choice of the closure method becomes much more important at high spatial resolution.

Equilibrium closures based on moisture convergence or on CAPE have originally been developed for global models and have been validated by large-scale field experiments. For mesoscale flow, however, there is no experimental indication of an instantaneous adjustment of convective and resolved dynamics and thus a non-equilibrium closure seems to be more appropriate. Also, in a potential unstable atmosphere, any forcing which lifts the air and brings it to saturation (e.g. turbulence or orographic lifting) will result in moist convection even if there is no low-level moisture convergence: Convection on the mesoscale is certainly not caused by large-scale water supply. On the other hand, the presence of convection may generate low-level moisture convergence due to induced subsidence in the cloud environment or due to mesoscale organization. Thus, a closure based on moisture convergence appears to be ill-posed as it violates causality. Since the fundamental cause of convection is conditional instability of the atmosphere, the closure method should depend somehow on the degree of this instability, e.g. being reflected in the amount of CAPE.

The formulation of the feedback relies on the assumption that the area fraction of a grid box covered by active convective cells is very small, implying that the compensating subsidence must take place within the same grid box. Clearly, at high model resolution this assumptions becomes dubious and can result in large errors in the feedback. A central future effort should consider the question of how to relax this assumption. Another point results from the nonhydrostatic modelling framework: the feedback should also formulate time-tendencies on vertical velocity and pressure perturbation. The latter is certainly difficult to realize as false acoustic and gravity waves may be generated by a non-isobaric feedback. But the extension to include the feedback on the vertical velocity seems to be straightforward. Especially, we expect a triggering effect from parameterized shallow convection to the onset of explicit deep convection.

Mass-flux schemes usually rely on a steady-state plume model for an ensemble of cumulus elements to calculate the redistribution of heat, moisture and horizontal momentum. These models are either spectral of bulk-type to take different cloud types into account. For high-resolution applications, these approaches can be abandoned: it is certainly sufficient to consider only one cloud-type on the

subgrid-scale. Also, the impact of sub-grid mesoscale organization can be neglected. This simplifies the formulation of the cloud model and more effort should be placed on a good representation of the interaction of the cloud-scale and the resolved flow.

In a steady-state plume model of type (35)-(36), entrainment and detrainment rates are specified which then determine the mass-flux profile. This is not realistic, as entrainment and detrainment are the consequence but not the cause of a vertical mass-flux variation: a change in the mass-flux results from a vertical acceleration which in turn causes entrainment or detrainment to take place because of mass continuity. In this way plume models will always fundamentally violate causality. An approach to overcome this drawback is to use a steady-state dynamic cloud model, which explicitly considers the vertical redistribution of vertical velocity. Dynamic entrainment and detrainment can then be diagnosed from the continuity equation. Also, an elaborated dynamic cloud model will give the feedback on vertical velocity in nonhydrostatic models in a natural way. This approach is currently considered within the COSMO-group, but the development is at the very beginning.

The vertical redistribution will also depend on the microphysics used in the cloud model. Generally, the parameterized cloud microphysics is very crude and efforts should be made to use more elaborated parameterizations. Also, a feedback should be formulated for all hydrometeors which are predicted by the grid-scale cloud scheme. This allows to consider subgrid-scale sources of e.g. cloud water, cloud ice, rain and snow resulting from their convective redistribution. Detrained particles such as cloud ice and snow can then be carried by the resolved motions and undergo phase changes on the grid-scale. This is important to allow for instance the formation of resolved anvils and anvil precipitation. Molinari and Dudek (1992) termed this the 'hybrid approach'. They stressed that the hybrid approach is essential for both the evolution of mesoscale convective structures driven by detrained hydrometeors and a smooth transition from convective-scale to grid-scale microphysics.

7.4 Convection at the meso-γ scale

In a couple of years, the LM is planned to be applied operationally for forecasts on the meso-γ scale by employing a grid spacing of 2-3 km. It is expected that deep moist convection and the feedback mechanisms to the larger scales of motion can then be resolved explicitly. For grid spacings less than about 3 km, this fully explicit approach is clearly superior to parameterized convection, since some of the doubtful constraints of parameterization schemes – e.g. the requirement of a scale gap in both space and time, or the assumption of cloud stationarity – can be overcome. However, even at a 2-3 km grid spacing only the rough structures of large convective clouds will be resolved.

In order to test the general behaviour of LM at very high horizontal resolution, a number of simulations using a 2.8-km grid spacing have been performed. Even if the physical package of the model in not yet appropriate for this scale and the initial and boundary conditions are not well defined (most of the simulations started with interpolated initial conditions from the 14-km grid DM), these tests give some indications on the capability to simulate deep convection explicitly. As an example, we consider here the 2 June 1999 case, where in the afternoon a severe squall line with hail and strong gusts formed over Germany. The strength of wind gusts caused a lot of damage, but came as a surprise since the squall-line system was not predicted by the operational models. On this day, a cyclone center was situated over British Isles and moved towards east. In the warm sector ahead of the cold front, first thunderstorms were triggered around 12 UTC over western France as isolated cells. By 14 UTC the thunderstorms start to organize in a squall line extending from the North sea to the Alps. Between 17 UTC and 18 UTC an arc-shaped organization of convective cells can be deduced from radar reflectivities in southern Germany (see Fig. 17, right). Strong wind gusts (around 100 km/h) were observed in that region.

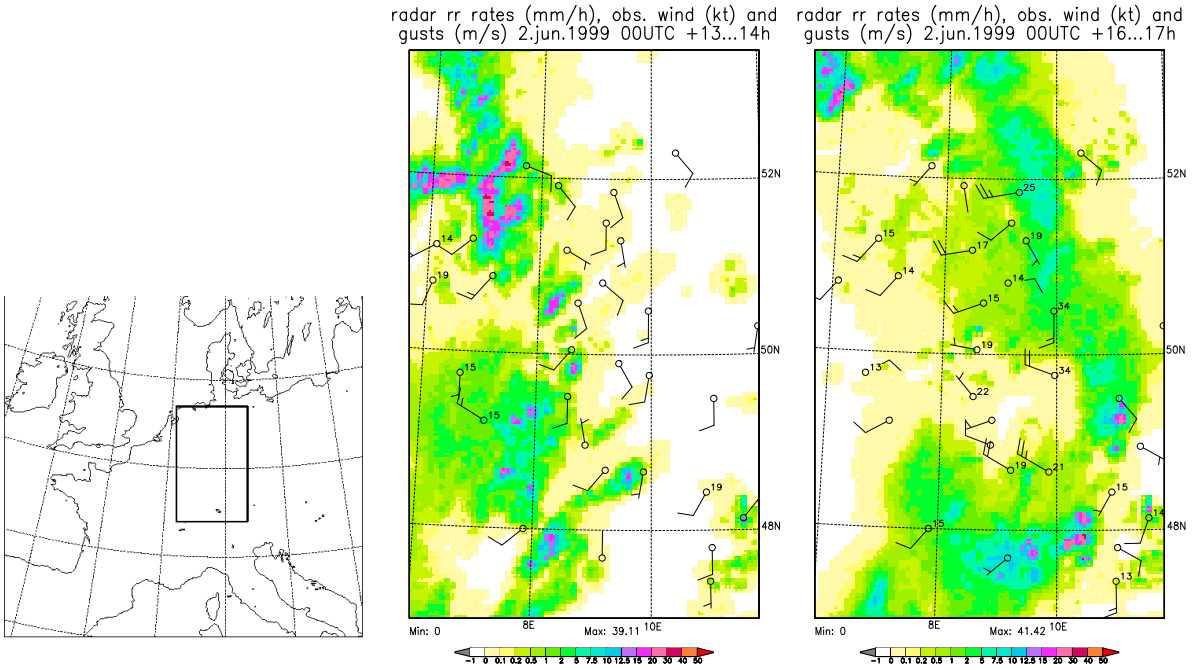

Figure 17: Left: Integration domain for the LM experiments with 7-km grid-spacing; the indicated subomain is used for the runs with 2.8-km resolution. Middle: 1-h precipitation rates derived from radar observations (mm/h) on the subdomain for 2 June 1999 13...14UTC. Wind barbs at Synop stations and 10-m gusts (numbers in kt) are also indicated. Right: same for 16...17 UTC.

Figure 18 shows the mean sea level pressure (pmsl) from three LM simulations for a subdomain extending from the North Sea to the northern ridge of the Alps in southern Germany: the LM reference run with 7-km grid spacing (left), a LM run with the same resolution but with convection scheme switched off (middle), and a LM run with 2.8-km resolution and explicit convection (convection scheme switched off, right). The forecast time is 17 hrs, corresponding to the time where the squall line was fully developed. As typical for squall lines, strong wind gusts will appear at the eastern boundary of a cold pool which originates due to precipitation evaporation. Cold air will cause a pressure rise resulting in the formation of a meso-high with large pressure gradients near the cold pool boundary. In the LM reference run, there is no indication for the formation of a meso-high. The failure of this forecast is due to parameterized convection using the Tiedtke scheme: In the simulation there is widespread weak convection within the warm sector, with a maximum around noon. Thus, the CAPE is released much too early, leaving no potential energy for the squall-line formation in the late afternoon. In contrast, a clear meso-high presence can be detected in the pmsl-field from the 2.8-km run, indicating a squall-line formation. The 7-km run with the convection scheme switched off shows also a signature of increased pressure gradient, but with a significant phase shift to the west. Available observed values of mean sea level pressure at Synop stations are included in figure; however, they are too sparse to verify the presence of a meso-high pressure system.

The structure of the pmsl-fields is reflected in the corresponding 10-m wind gusts plotted in Fig. 19. A clear, fully resolved gust front is present in the 2.8-km LM run. The values verify well with the magnitude of the observed wind gusts that are included in figure (up to 100 km/h). When compared to the measurements, the simulated squall line has moved slightly too fast to the east. The shape of the gust front looks surprisingly similar to the squall-line shape shown in radar precipitation intensity field (Figure 17, right). Increased wind speeds are also present in the 7-km no-convection-scheme run, but with smaller values. Also, the propagation of the squall line appears

to be retarded. Corresponding plots of isosurfaces of cloud water content (not shown) for the 2.8-km run indicate deep convective clouds at various development stages oriented in a line-structure, which is very similar to the observed arc-shaped band of precipitation in Fig. 17.

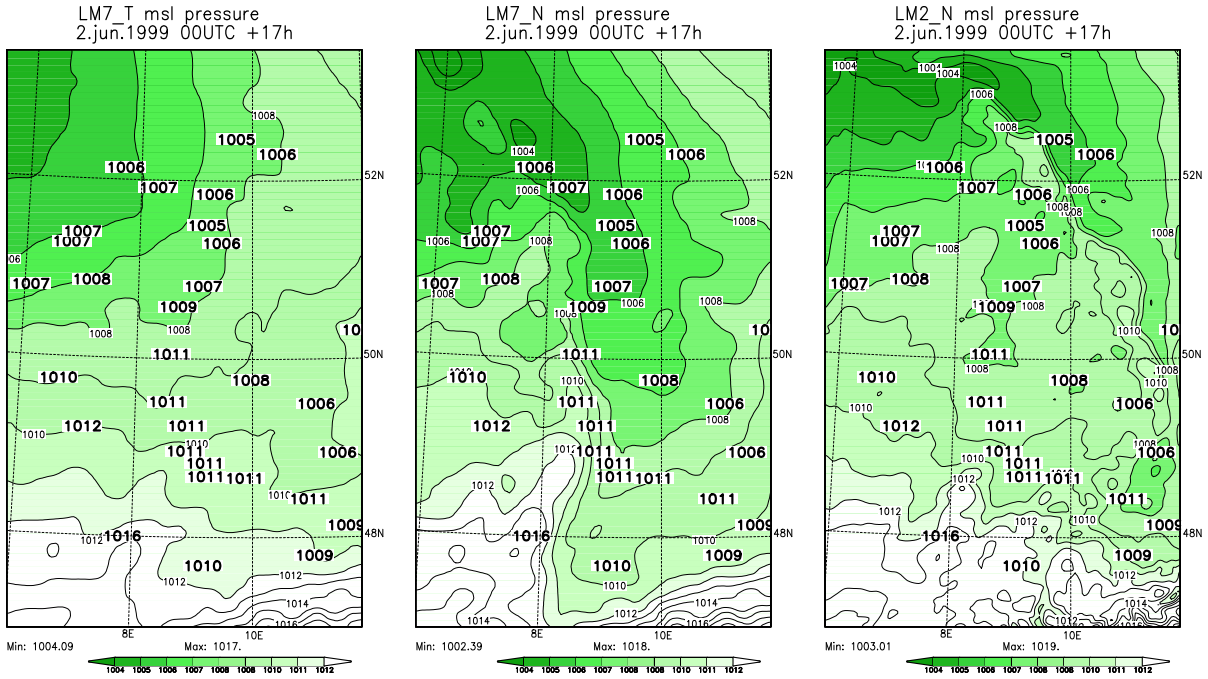

Figure 18: Observed mean sea level pressure (numbers in hPa) and forecasted pmsl from the 7-km reference run (left), the 7-km run with the convection scheme switched off (middle) and the 2.8-km run (right); valid on 2 June 1999 17UTC.

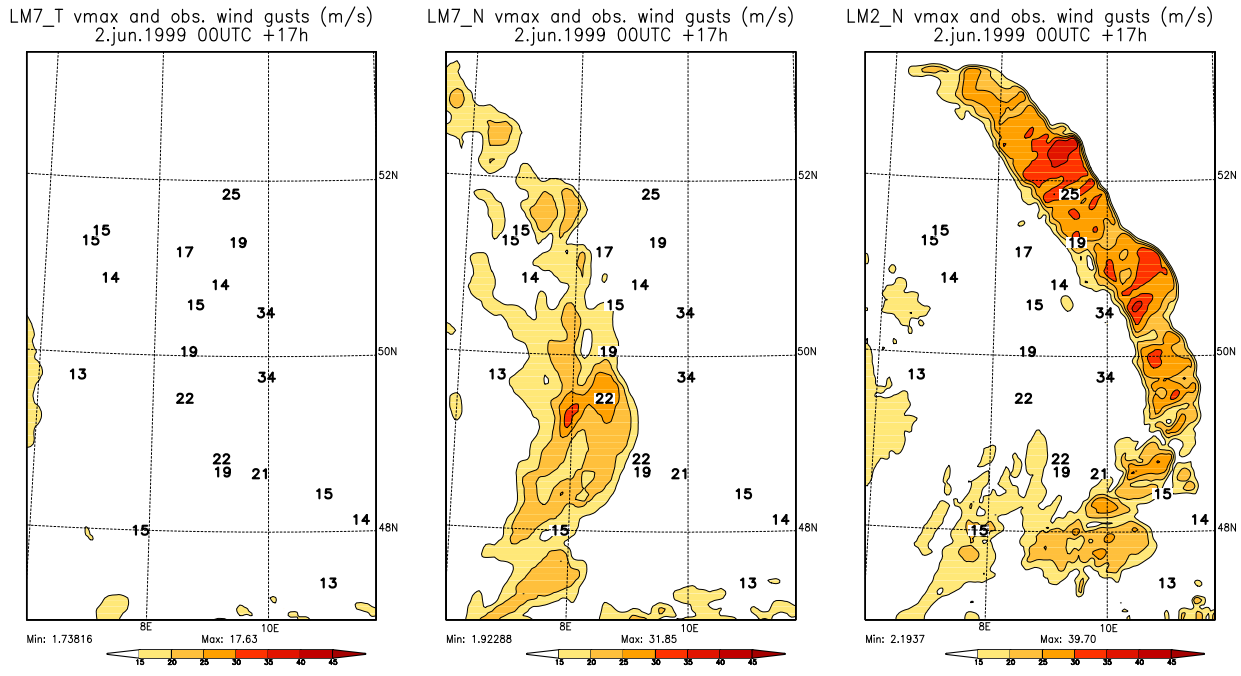

Figure 19: Observed wind gusts (numbers in kt) and forecasted 10-m wind gusts from the 7-km reference run (left), the 7-km run with the convection scheme switched off (middle) and the 2.8-km run (right); valid on 2 June 1999 17UTC.

The results indicate that deep moist convection can be simulated quite realistically by using the LM without parameterized convection at high spatial resolution – at least for this test case with strong synoptic-scale forcing. The LM with 7-km resolution is able to simulate convective cells explicitly though at the wrong scale and not very realistically. At 2.8-km resolution the simulation of deep convective cells is much more realistically. Also the basic feed-back mechanisms of convection as well as interactions with the larger scales, which result in the formation of a squall-line structure with corresponding pressure patterns, appear to be well represented.

For cases with weak synoptic-scale forcing, however, the experimental 2.8-km version of LM sometimes fails to reproduce or significantly delays the observed development of air-mass thunderstorms, especially over flat terrain. This indicates that certain mechanisms triggering the onset of a resolved vertical circulation in such situations are missing. A canditate for such triggering is shallow convection, which is still sub-grid scale and of course is not represented when we simply switch off the model's convection scheme. The current large-scale parameterization scheme cannot be used for this purpose: Leaving this scheme switched on results in an unrealistic evolution of convective precipitation in both space and time, and inhibits the formation of explicitly resolved cells due to quasi-instantaneous removal of CAPE. Thus, the development of a new parameterization scheme for shallow convection, which is able to trigger the initiation of deep moist convective cells by a smooth transition from parameterized to explicitly resolved cell circulations, appears to be a demanding future task in high-resolution modelling.

8 A New Multi-Layer Soil-Model

For land surfaces, the LM soil model TERRA provides the surface temperature and the specific humidity at the ground. The ground temperature is calculated by solving the equation of heat conduction with the EFR (extended force-restore) method after Jacobsen and Heise (1982). Two soil layers with adjusted depths for optimal response to dual frequency harmonic forcing are used. In practical application, there are three major shortcomings of this scheme: (i) the thermal thickness of the soil layers depends on soil type, (ii) different thicknesses have to be used for water transport, resulting in an inconsistent interaction of thermal and hydrological transport, and (iii) due to the relatively large thickness of the upper soil layer, freezing and melting of soil water has to be excluded in order to avoid a significant suppression of temperature changes if phase transitions occur. This, on the other hand, enhances the temperature response in an unrealistic way.

Thus a new multi-layer version (TERRA_LM) has been developed which is based on the direct numerical solution of the heat conduction equation (HCE-method). With the HCE-method, the soil can rapidly react to high frequency changes of the atmospheric forcing. A great advantage of the multi-layer version is the formulation of hydrological and thermal processes with exactly the same layer distribution, simplifying the formulation of feedback processes between the thermal and hydrological parts of the model. A major improvement results also from the inclusion of phase transitions in the soil layers.

Numerical experiments have shown that six active layers with increasing thicknesses of 0.01, 0.03, 0.06, 0.12, 0.24 and 0.48 m from top to bottom are sufficient for numerical weather prediction models. The results become useless if the the number of active layers is reduced to less than four, and with additional layers close to the soil surface the results do not differ remarkably, even if freezing and melting occurs. A seventh inactive layer, the so-called climate layer, is added with prescribed temperature and water content. Figure 20 shows the structure of the new soil model.

Two versions for the representation of phase transitions in the soil layers have been implemented:

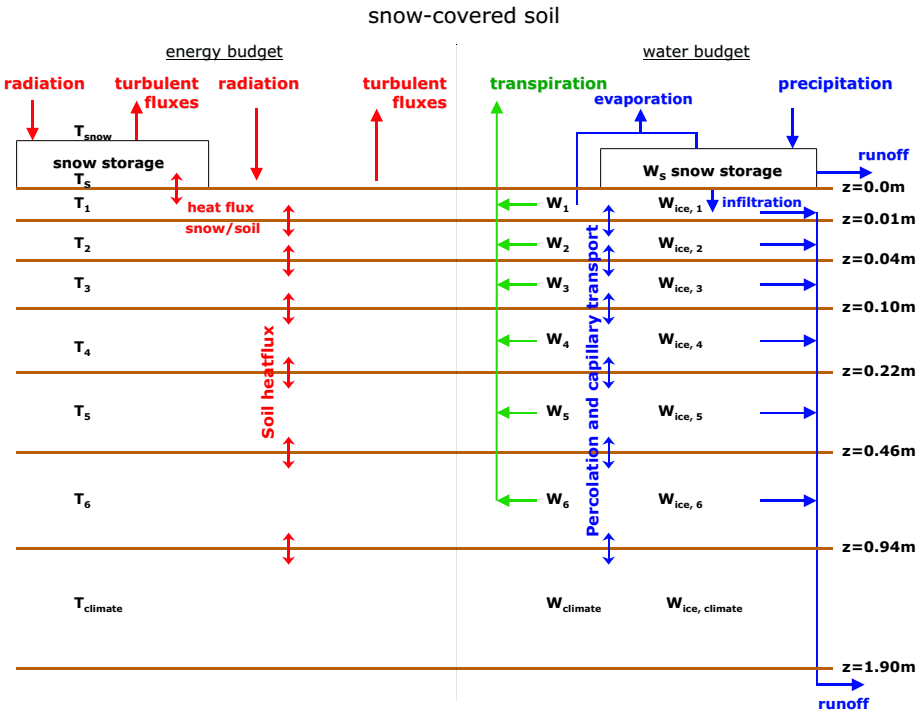

Figure 20: The multi-layer grid of the soil model TERRA_LM: General structure and physical processes considered in case of a snow covered soil.

(a) freezing and melting occurs at a threshold temperature T_{thr} equal to the freezing point $T_0 = 0°C$; this gives the maximum effect of phase transitions.

(b) freezing and melting occurs at a threshold temperature T_{thr} depending on soil water content and soil type following Flerchinger and Saxton (1989); this gives the minimum effect of phase transitions. For details of this formulation, see Schrodin and Heise (2001).

To investigate the general effect of freezing/melting and especially the effect of the two different definitions of the threshold temperature, one dimensional simulations with a stand alone soil model were performed. In all test cases an artificial diurnal cycle of the thermal forcing at the soil surface is prescribed. A vertically constant temperature profile is assumed initially, and the integrations are repeated cyclically until a quasi-stationary state is reached. As no analytical solution of the heat conduction equation is available for this type of experiments, a 200-layer-version of the multi-layer soil model with layer thicknesses of 0.005 m is used as a reference. In all cases the soil-type loam is used. Simulations for three different values of the soil water content (0.8 W_{por}, 0.5 W_{por}, 0.2 W_{por}, vertically constant) are performed.

In Figure 21 the results with $T_{thr} = T_0$ are shown. In the 200-layer-version (left) with high values of soil water content (0.8 W_{por}) the soil surface temperature remains at T_0 for a considerable part of the day. Compared to a run without freezing/melting the temperature amplitude is reduced by about 70 %. With decreasing soil water content the duration of the periods with surface temperatures fixed to T_0 decrease and the amplitude of the diurnal temperature curve increases. If the freezing/melting of one layer has been completed, the temperature can decrease/increase until the next layer starts with this process, fixing the surface temperature again, now on a deeper/higher temperature. Of course this effect is coarsened in the 6-layer-version (Figure 21, right). The freezing/melting of the

second layer now also forces the surface temperature to be fixed to a quasi constant value over some hours if the soil water content is rather high. Taking the results of the 200-layer-version as the truth, temperature amplitudes are somewhat too large in the 6-layer-version.

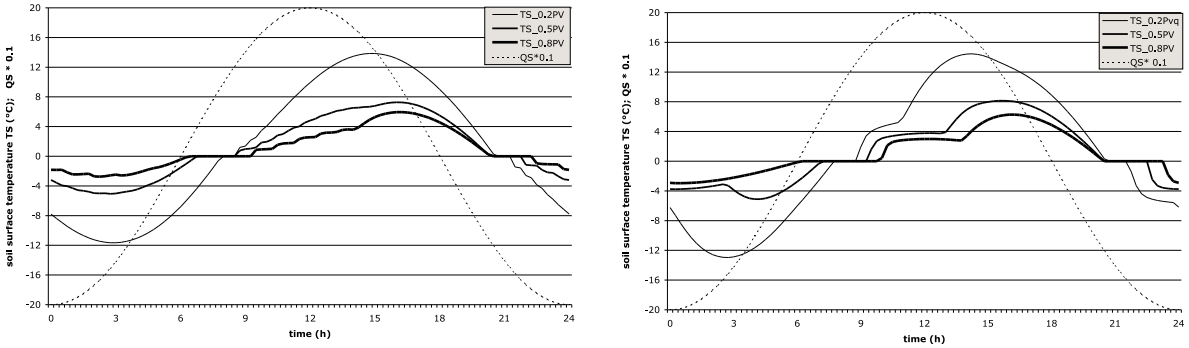

Figure 21: Soil surface temperature (°C) for a harmonic thermal forcing (dotted) and different water contents (see text). Freezing and melting at freezing point. Left: 200-layer version. Right: 6-layer version.

If instead of $T_{thr} = T_0$ we use the water content dependent threshold temperature, the effect of freezing/melting is reduced very much (Figure 22). Now there is no effect at all in the case of a dry soil as this low water content can not freeze until the temperature is extremely low. For the wetter soils, the periods of quasi constant surface temperature are much shorter compared to the version with $T_{thr} = T_0$, both in the 200-layer (Figure 22, left) and in the 6-layer version (Figure 22, right). In general this gives the temporal course of temperature a somewhat smoothed appearance.

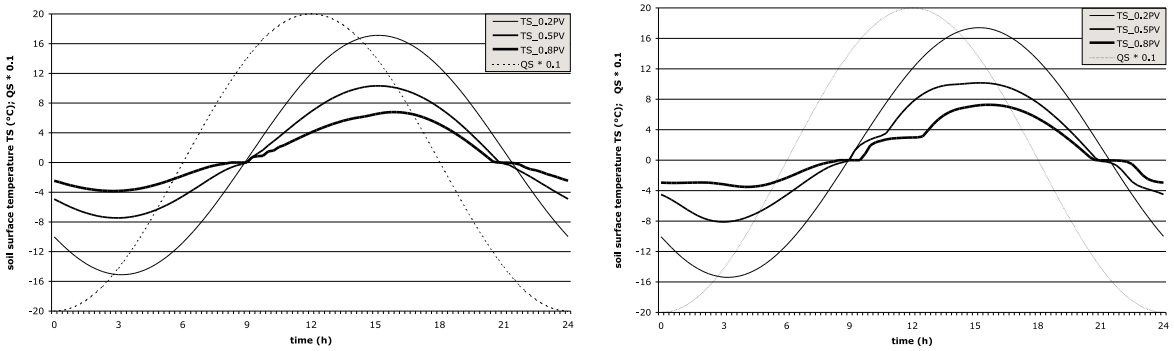

Figure 22: Soil surface temperature (°C) for a harmonic thermal forcing (dotted) and different water contents (see text). Freezing and melting at a threshold temperature depending on soil moisture and soil type. Left: 200-layer version. Right: 6-layer version.

These tests show that the inclusion of freezing/melting has a significant effect on the soil surface temperature. In this aspect, the HCE-method performs superior to the former EFR-method and in practical applications a beneficial impact in the prediction of 2m-temperature during the early and late winter season is expected (the operational application of the multi-layer soil model is scheduled for spring 2002). The two different methods to calculate phase transitions in the new multi-layer

soil model, however, give significantly different results. It will be left to modelling experience with daily temperature verification to decide about the right way to include freezing/melting effects.

9 Filtering of Topography

A long-standing problem in high-resolution modelling is the prediction of unrealistic precipitation fields in mountainous areas. During the first year of the operational NWP-application of LM, two main deficiencies became evident: (i) extremely large amounts of precipitation occur directly over mountain tops and (ii) at the same time deep valleys and mountain lee-sides receive no precipitation at all, turning into a desert-like climate in the model's assimilation cycle. These effects are most noticeable over the Alpine region, but are also noticeable over mid-range mountain areas. All in all, the predicted precipitation fields look very noisy in regions with steep topography.

A reason for this behaviour is the use of mean topography at the grid-scale Δx, which will result in 'singular' mountain tops and valley grounds being represented by one gridpoint only. Constant dynamical surface forcing of this type introduces a hopelessly inaccurate numerical feedback to the simulated flow, which then can affect the physics in a strange way. To investigate this effect, convergence tests of the solutions corresponding to mountain generated 3-D gravitational waves have been performed (Gassmann, 2001). The conclusion of these tests is that topographical structures must be reasonably well resolved by the grid in order to obtain a quantitatively correct flow. Similar tests have been performed by Davies and Brown (2001) for a 2-D flow.

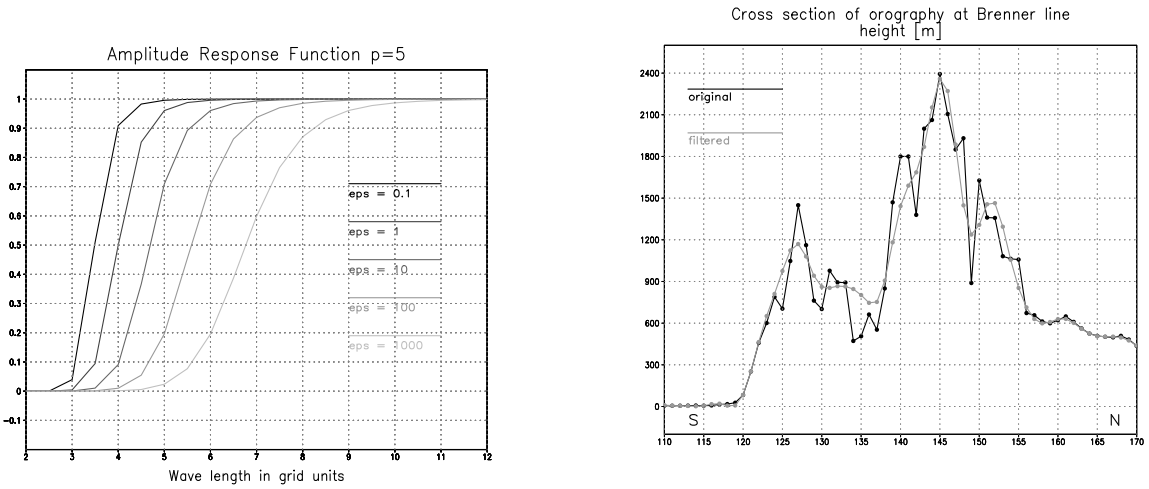

Figure 23: Left: Amplitude response function of the 10-th order Raymond filter for various values of the filter parameter ϵ. Right: South-north cross section of the LM-topography along the Brenner line for original (black) and filtered (grey) topography.

Thus a weak filtering of topography, i.e. a removal of the very small-scale components from the wave spectrum, is necessary to allow for a more correct interaction of the dynamics with the surface. A 10-th order Raymond (1988) filter using a filter parameter of $\epsilon = 0.1$ is applied for this purpose. Figure 23 (left) shows the amplitude response function for this filter. $2\Delta x$ and $3\Delta x$ wave components are filtered almost completely whereas $4\Delta x$ and larger scale components remain untouched. The impact of this weak filter on the LM topography is also shown in Figure 23 (right): all singular mountain and valley structures are removed.

The use of a filtered topography has a dramatic impact on the predicted precipitation field. An example is shown in Figure 24 for a test simulation starting at 8 February 2000 00 UTC. The

routine run (right) exhibits the well known features with unrealistic minima and maxima of the 24-h accumulated precipitation amount in the Alps. A much smoother spatial distribution is predicted in the experimental run with filtered topography. All larger scale patterns and the area mean value of precipitation are very similar compared to the routine run, whereas the maximum and the variance of precipitation is reduced by about a factor of 2. Outside the mountainous Alpine region, the differences are negligible.

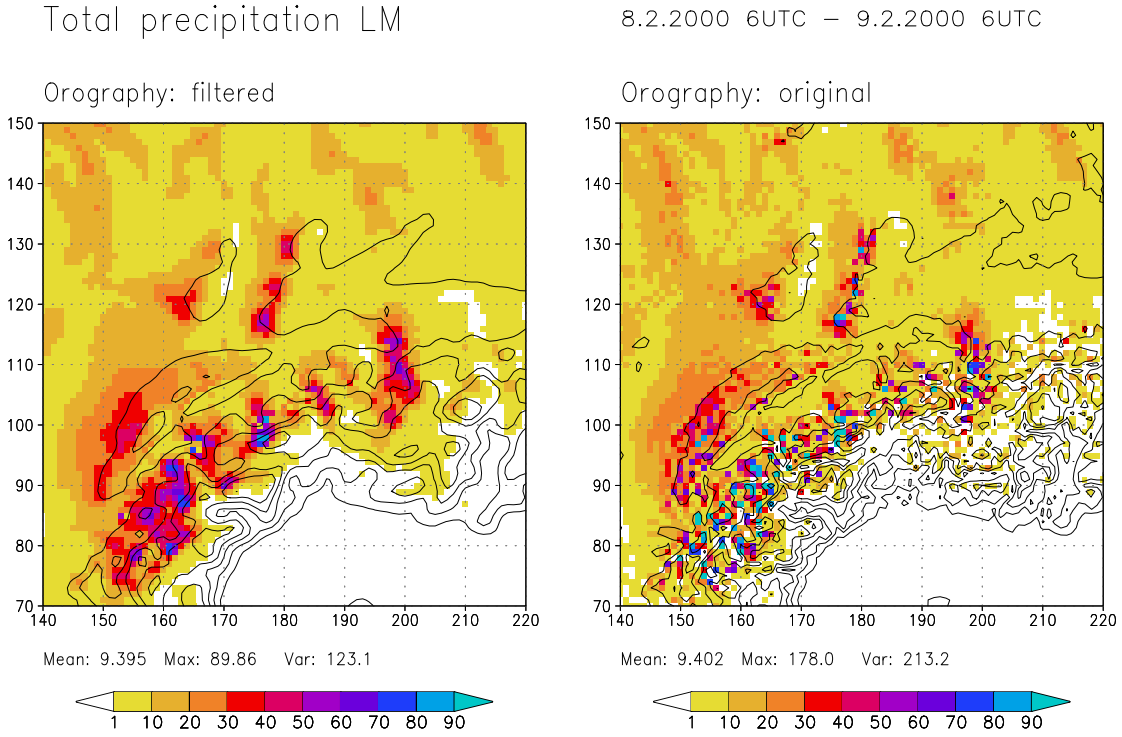

Figure 24: 24-h precipitation amount of a LM simulation starting at 8 February 2000 00 UTC. Left: Experimental run with filtered topography. Right: Operational run with unfilterd topography.

Results from other simulations and the statistical evaluation of a quasi-operational test suite revealed an overall positive impact of using a weakly filtered orography. In general, there is no loss of meteorological relevant information and the precipitation patterns appear to be more realistic. We conclude that filtering of topography is necessary to avoid the formation of non-coherent dynamical structures generated by under-resolved surface forcing. Since December 2000, the operational runs with LM use a filtered topography.

10 Horizontal Diffusion with an Orographic Limiter

NWP models require numerical smoothing to damp small-scale ($2\Delta x$) noise being related to stepwise or singular signals which are permanently generated in a nonlinear model. The usually applied regular 4th-order linear diffusion, however, tends to introduce unphysical solutions and thus new noise on the resolvable scales which then can erroneously drive physical processes. In order to achieve monotonic and mass-conserving numerical diffusion, a new scheme based on direct multi-dimensional flux-limiting has been constructed (Doms, 2001). The scheme is based on the work of Xue (2000) but the formulation of the monotonic flux-limiter follows Smolarkiewicz (1989).

Tests with 1-D and 2-D idealized cases have shown a beneficial impact of the new scheme. All over- and undershoots – as typical for regular 4th-order diffusion – are removed from the solution

and a strictly monotonic solution is guaranteed. In LM simulations of real cases considered so far, however, there is only a relatively small impact from using monotonic 4th order diffusion with a tendency for lower vertically integrated cloud water and smaller peak precipitation amounts.

A more severe problem results from the fact that numerical smoothing is usually realized as horizontal diffusion, i.e. along surfaces of constant vertical coordinate. Since most NWP models use a terrain-following vertical coordinate, this will result in systematic numerical biases, as an unwanted vertical mixing in physical space is implied. This type of numerical error will increase nonlinear with increasing steepness of the topography, and thus poses a severe problem in high-resolution regional models. Well known remedies, such as doing diffusion on z- or p-surfaces or applying a local reduction of the diffusion coefficients, are not mass-conserving and will introduce other uncontrollable errors. With the new smoothing scheme, the topography-induced biases can be reduced without violating mass conservation while still maintaining monotonicity by simply applying an orographic limiter to the diffusive fluxes at cell interfaces. As limiter function we suggest a simple quadratic decrease of the fluxes with increasing height difference between neighboring gridpoints. Beyond a threshold value of the height difference (currently 250m for the 7 km grid spacing used in LM), the fluxed are set to zero.

Test integrations with the orographic limiter have been performed for a number of cases from the period October-November 2000. During this time, a synoptic-scale weather situation with southerly flow over the Alps prevailed, often causing a Föhn flow in regions to the north of the Alps which blocked or weakened of cold fronts approaching from the west. In the operational forecasts with the LM, however, the Föhn-effect was overestimated in many cases, resulting in a severe underprediction of precipitation for southwestern Germany and the northern parts of Switzerland. The experiment revealed that horizontal diffusion has a large dynamical impact on the onset and strength of Föhn flow. As an example, we choose here the forecast starting from 00 UTC at 11 October 2000.

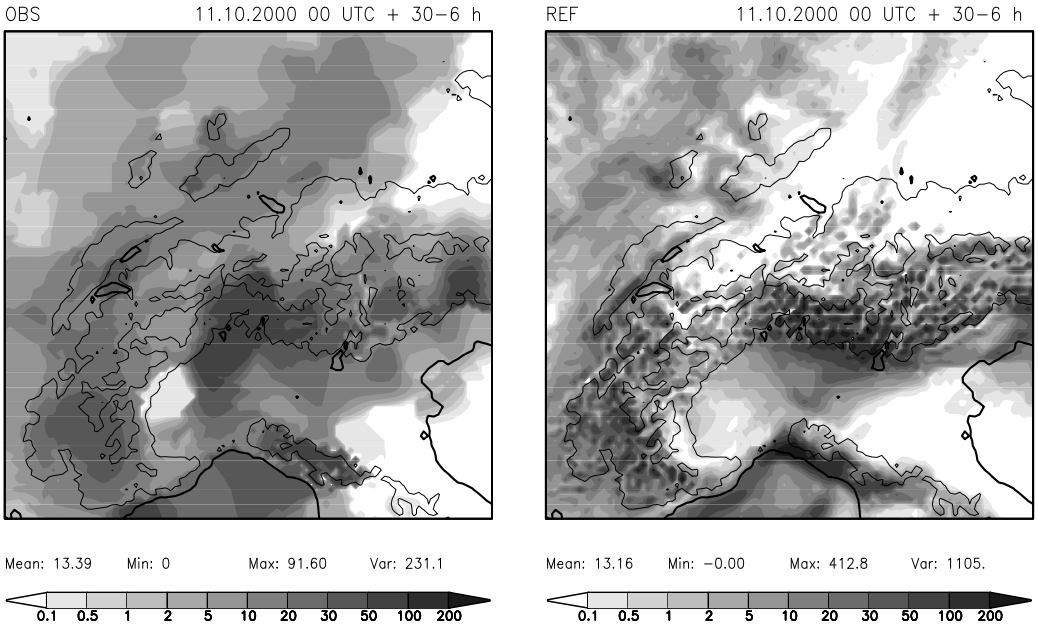

Figure 25: 24-h accumulated precipitation (mm) for 11 October 2000 00 UTC +06h ...+30h. Left: Analysis based on Synop observation; the thick contour lines show the land-sea mask, the thin lines are the 700m and 2100m contour lines of orography. Right: Reference run.

Fig. 25 compares the 24-h accumulated precipitation amount from the reference run (right) and from the Synop observations (left) on a model subdomain covering the Alpine region. As the

observation come from the rather coarse SYNOP network, the structure of the precipitation field is only a first guess and many details may be lost. Nevertheless, the observation indicate a large region along the southern ridge of the Alps with precipitation amounts in the range 50 - 100 mm (which resulted in a severe flooding event in the Turin region). This is well captured by the model forecast, the centre is shifted somewhat to the east. The peak precipitation, however, is certainly overestimated by the model. Another region with high precipitation amounts is along the western ridge of the alps, but also here the peak values seem to be too high. In general, the forecasted precipitation field looks very noisy, with $2\Delta x$ structures located in regions of steep topography. This is not believed to be realistic.

The overestimation of blocking by southerly Föhn flow is obvious in the northern part of the Alps: whereas the observations indicate precipitation amounts in the range of 5 - 20 mm in a region extending from the Lake of Geneva over the Lake of Constance into the southwestern parts of Bavaria, the forecast gives almost no indication of precipitation, except for a spotty structure over northern Switzerland. Another typical feature of many LM precipitation forecasts can also be noticed: The valley of Valais, a steep valley extending southeast of the Lake of Geneva, remains almost dry, whereas a large amount of rain and snow is simulated over the mountain tops at the valley sides. The observations, however, indicate significant precipitation at the valley ground.

The use of orographically limited horizontal diffusion has a remarkable impact on the flow field in the Alpine region and thus on the predicted precipitation amount. The left picture in Fig. 26 displays the result obtained with new scheme. When compared to the reference run, the precipitation pattern looks less noisy than in the reference run and a part of the $2\Delta x$ structures are gone or their amplitude appears to be smaller: the field variance is reduced from 1105 mm down to 853 mm and the field maximum from 413 mm to 338 mm. Also, the southwest-northeast orientation of the small-scale precipitation bands over the western parts of the Alps has changed to a more northwest-southeast orientation. As a distinct feature of the new scheme, the "dry valley effect" seems to be cured: with flux-limited horizontal diffusion a significant precipitation amount is now predicted for the valley of Valais. Most interestingly, a coherent rainband extending from northern Switzerland to western Bavaria is now formed, with an eastern boundary close to the observed one. Clearly, a large part of precipitation is still missing to the west of this band, but this experiment indicates that a too strong horizontal diffusion over steep terrain can have significant dynamical impact to the fields far away.

This test case has been run with the original mean topography at the grid scale. Since the filtered orography (see Section 9) is smoother and less steep, the errors from horizontal diffusion are expected to become smaller. And indeed, a rerun with the new smoothing scheme including topographical filtering reveals a further improvement of the flow structure. The right hand picture in Fig. 26 displays the corresponding 24-h precipitation amount. The precipitation field becomes less noisy, and the rainband appears to be slightly broader and more intense.

This and other test simulations with the orographical limiter revealed a noticeable improvement of topographical flow structures. The spatial distribution of rain over mountainous areas appears to be much less noisy and the peak values over mountain tops are significantly reduced compared to the reference runs with standard 4th-order horizontal diffusion. Also, the dry valley effect is removed and the model's tendency for blocking frontal precipitation north of the Alps is weakened. Following these case studies, parallel test experiments with the modified horizontal diffusion scheme have been conducted for one month time periods at MeteoSwiss (November 2000) for interpolated GME initial conditions and at DWD (August 2001) using the full LM data assimilation cycle. The statistical evaluation of both test suites against observed surface weather parameters revealed a neutral impact of the new smoothing scheme to most parameters, with a marginal improvement of cloud cover and surface layer humidity. The scores for the 6-h accumulated precipitation, however,

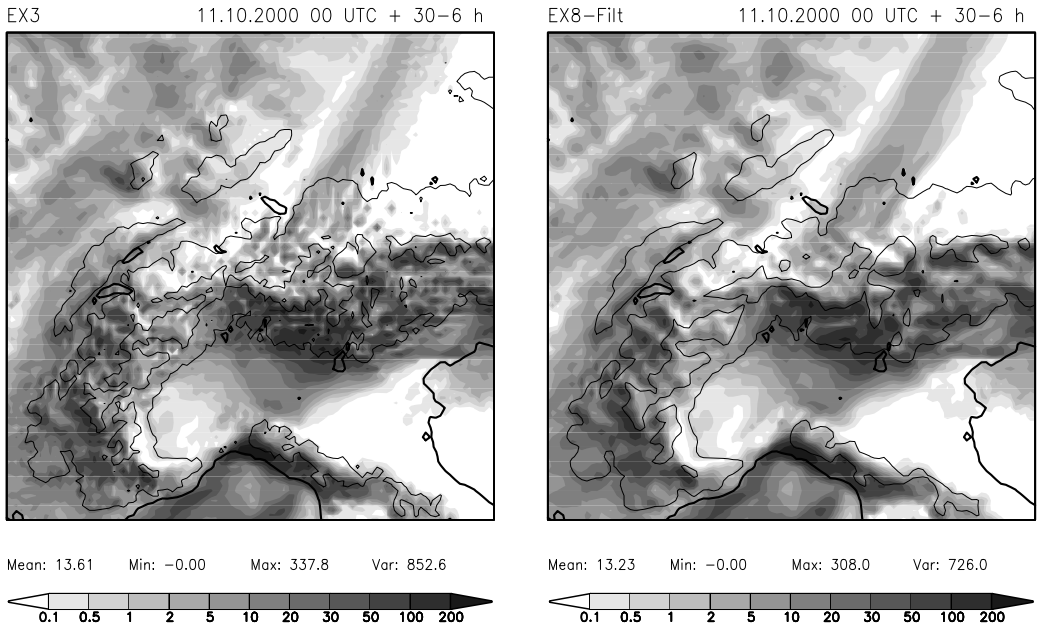

Figure 26: As in Fig. 25 but for the orographically limited monotonic diffusion scheme (left). Right: The same scheme, but for the filtered orography.

improved significantly for higher threshold values (> 2mm/6h), indicating a more reliable prediction of heavy precipitation events.

11 Summary and Plans

The LM is a nonhydrostatic limited area model for high-resolution numerical weather prediction. Both the model formulation and the data assimilation scheme have been briefly summarized. A number of new and unique parameterization schemes have been developed to improve the operational forecasts on the meso-β scale. A part of these schemes is already running successfully in the operational application of the model, others are being tested in a pre-operational mode.

The new LM scheme for vertical diffusion is based on prognostic turbulent kinetic energy. Compared to traditional K-closure, a significant improvement could be achieved, mainly due to the inclusion of subgrid thermal circulations and by taking into account effects from subgrid cloud condensation and evaporation. Also, the new surface layer scheme with viscous sub-layer contributes to a more accurate prediction of near-surface parameters such as 2-m temperature and dew point, and 10-m wind. For future model applications at higher resolution, also lateral turbulent fluxes, e.g. at cloud boundaries, must be considered. The extension of the present TKE-scheme to allow for 3-turbulence appears to be straightforward.

A new microphysics scheme for grid-scale clouds and precipitation has been developed. It is based on separate prognostic equations for both cloud water and cloud ice. In contrast to many other ice-phase schemes, the depositional growth of cloud ice and of snow is formulated as a non-equilibrium process. This avoids the traditional but unphysical assumption of thermodynamic equilibrium of both water and ice substance at sub-freezing temperatures, and allows for an explicit representation of precipitation enhancement due to mechanisms such as the Bergeron-Findeisen and the Seeder-Feeder processes. Test simulations with the new scheme have revealed an overall beneficial impact, especially with respect to high-level cloudiness and anvil formation. A good treatment of ice-phase

processes will be also important for an explicit simulation of deep convection. In this aspect, we plan to include graupel and hail in a future version of the scheme. Furthermore, 3-d advection of precipitating hydrometeors becomes significant at high resolution. Preliminary tests with a prognostic treatment of rain and snow revealed that horizontal transport becomes non-negligible at grid-spacings below 10 km.

At high spatial resolution, an accurate numerical treatment of topographical forcings becomes of much more importance than in coarse-grid models. Errors resulting from an under-resolved topography or from horizontal diffusion along sloping coordinate surfaces can drive physical processes in mountainous regions, which will result in unrealistic forecasts. To remedy this problem, we use a filtered topography and a new scheme for horizontal diffusion with an orographic flux-limiter. A more long-term LM project aims at the replacement of the current terrain-following coordinates by an orthogonal z-coordinate system with finite-volume shaved-element discretization.

12 References

Arakawa, A. and W. H. Schubert, 1974: Interaction of a cumulus cloud ensemble with the large-scale environment. *J. Atmos. Sci*, 31, 674-701.

Bower, K. N., S. J. Moss, D. W. Johnson, T. W. Choularton, J. Latham, P. R. A. Brown, A. M. Blyth and J. Cardwell, 1996: A parameterizaion of the ice water content observed in frontal and convective clouds. *Quart. J. Roy. Meteor. Soc.*, 122, 1815-1844.

Davies, H. C. and R. E. Turner, 1977: Updating prediction models by dynamical relaxation: An examination of the technique. *Quart. J. Roy. Meteor. Soc.*, 103, 225-245.

Davies, L. A. and A. R. Brown, 2001: Assessment of which scales of orography can be credibly resolved in a numerical model. *Quart. J. Roy. Meteor. Soc.*, 127, 1225-1237.

Doms, G., U. Schättler, 1999: The Nonhydrostatic Limited-Area Model LM (Lokal-Modell) of DWD. Part I: Scientific Documentation. Deutscher Wetterdienst (DWD), Offenbach (available at www.cosmo-model.org).

Doms, G., 2001: A scheme for monotonic numerical diffusion in the LM. *Cosmo Technical Report*, No.3 (available at www.cosmo-model.org).

Dudhia, J., 1993: A nonhydrostatic version of the Penn State / NCAR mesoscale model: Validation tests and simulation of an Atlantic cyclone and cold front. *Mon. Wea. Rev.*, 121, 1493-1513.

Feigelson, E. M., 1978: Preliminary radiation model of a cloudy atmosphere. Part I: Structure of clouds and solar radiation. *Beitr. Phys. Atmos*, 51, 203-229.

Flerchinger, G. N. and K. E. Saxton, 1989: Simultaneous heat and water model of freezing snow-residue-soil system. I. Theory and development. *Transactions of the ASEA*, 32, 2, 565 - 571.

Fritsch, J. M. and C. F. Chappell, 1980: Numerical prediction of convectively driven mesoscale pressure systems. Part I: Convective parameterization. *J. Atmos. Sci.*, 37, 1722-1733.

Gassmann, A., 2001: Filtering of LM-Orography. *COSMO Newsletter*, No.1, 71-78 (available at www.cosmo-model.org).

Gassmann, A., 2001: Prognostische Niederschlagsbehandlung im LM. *DWD Forschung und Entwicklung, Arbeitsergebnisse*, Nr. 66, Deutscher Wetterdienst, Offenbach.

Ghan, S. and R. Easter, 1992: Computationally efficient approximations to stratiform cloud and microphysics parameterization. *Mon. Wea. Rev.*, 120, 1572-1582.

Gregory, D. 1995: The representation of moist convection in atmospheric models. *Parameterization of sub-grid scale physical processes.*. ECMWF Seminar Proceedings, Reading, UK.

Gregory, D. and P. R. Rowntree, 1990: A mass-flux convection scheme with representation of cloud ensemble

characteristics and stability-dependent closure. *Mon. Wea. Rev.*, 118, 1483-1506.

Hess, R., 2001: Assimilation of screen-level observations by variational soil moisture analysis. *Meteor. Atmos. Phys.*, 77, 155-166.

Hobbs, P. V. and A. L. Rango, 1985: Ice particle concentrations in clouds. *J. Atmos. Sci.*, 42, 2523-2549.

Jacob, C. and S. A. Klein, 1999: The role of vertically varying cloud fraction in the parameterization of microphysical processes in the ECMWF model. *Quart. J. Roy. Meteor. Soc.*, 125, 941-965.

Jacobsen, I. and E. Heise, 1982: A new economic method for the computation of the surface temperature in numerical models. *Contr. Atmos. Phys.*, 55, 128-141.

Kessler, E., 1969: On the distribution and continuity of water substance in the atmospheric circulations. *Meteor. Monogr.*, 10, No. 32, Amer. Met. Soc., 84pp.

Klemp, J. B. and R. Wilhelmson, 1978: The simulation of three-dimensional convective storm dynamics. *J. Atmos. Sci.*, 35, 1070-1096.

Kuo, H.-L., 1974: Further studies of the parameterization on the influence of cumulus convection on large-scale flow. *J. Atmos. Sci.*, 31, 1232-1240.

Lin K. N., R. D. Farley and H. D. Orville, 1983: Bulk-parameterization of the snow field in a cloud model. *J. Clim. Appl. Meteor.*, 22, 1065-1092.

Lin, S.-J. and R. B. Rood, 1996: Multidimensional flux-Form semi-Lagrangian transport schemes. *Mon. Wea. Rev.*, 124, 2046-2070.

Louis, J.-F. 1979: A parametric model of vertical eddy fluxes in the atmosphere. *Bound. Layer Meteor.*, 17, 187-202.

Lynch. P., D. Girard and V. Ivanovici. 1997: Improving the efficiency of a digital filtering scheme. *Mon. Wea. Rev.*, 125, 1976-1982.

Mellor, G. L. and T. Yamada, 1974: A hierarchy of turbulence closure models for planetary boundary layers. *J. Atmos. Sci.*, 31, 1791-1806.

Mellor, G. L. and T. Yamada, 1982: Development of a turbulence closure model for geophysical flow problems. *Rev. Geophys. and Space Phys.*, 20, 831-857.

Myers, M. P., P. J. DeMott and W. R. Cotton, 1992: New primary ice-nucleation parameterization in an explicit cloud model. *J. Appl. Meteor.*, 31, 708-721.

Molinari, J. and M. Dudek, 1992: Parameterization of convective precipitation in mesoscale numerical models: a critical review. *Mon. Wea. Rev.*, 120, 326-344.

Raupach, M. R. and R. H. Shaw, 1981: Averaging procedures for flow within vegetation canopies. *Bound. Layer Meteor.*, 22, 79-90.

Raymond, W. H., 1988: High-order low-pass implicit tangent filters for use in finite area calculations. *Mon. Wea. Rev.*, 116, 2132-2141.

Rasch, P. J., and J. E. Kristjansson, 1998: A comparison of the CCM3 model climate using diagnosed and predicted condensate parameterizations. *J. Clim.*, 11, 1587-1614.

Raschendorfer M. and D. Mironov, 2001: Evaluation of empirical parameters of the new LM surface-layer parameterization scheme. Results from numerical experiments including the soil-moisture analysis. *Cosmo Technical Report*, No.1 (available at www.cosmo-model.org).

Ritter, B. and J.-F. Geleyn, 1992: A comprehensive radiation scheme for numerical weather prediction models with potential applications in climate simulations. *Mon. Wea. Rev.*, 120, 303-325.

Rutledge, S. A. and P. V. Hobbs, 1983: The mesoscale and microscale structure and organization of clouds and precipitation in mid-latitude cyclones. VIII: A model for the 'seeder-feeder' process in warm-frontal cloud bands. *J. Atmos. Sci*, 40, 1185-1206.

Ryan, B. F. 1996: On the global variation of precipitating layer clouds. *Bull. Americ. Met. Soc.*, 77, 53-70.

Schraff, C., 1997: Mesoscale data assimilation and prediction of low stratus in the Alpine region. *Meteor. Atmos. Phys.*, 64, 21-50.

Schrodin, R. and E. Heise (2001): The Multi-Layer Version of the DWD Soil Model TERRA_LM. *Cosmo Technical Report*, No.2 (available at www.cosmo-model.org).

Skamarock, W. C. and J. B. Klemp, 1992: The stability of time-split numerical methods for the hydrostatic and the nonhydrostatic elastic equations. *Mon. Wea. Rev.*, 120, 2109-2127.

Smith, R. N. B., 1990: A scheme for predicting layer clouds and their water content in a general circulation model. *Quart. J. Roy. Meteor. Soc.*, 116, 435-460.

Smolarkiewicz, P. K., 1989: Comment on "A positive definite advection scheme obtained by nonlinear renormalization of the advective fluxes". *Mon. Wea. Rev.*, 117, 2626-2632.

Sommeria, G. and J. W. Deardorff, 1977: Subgrid-scale condensation in models of non-precipitating clouds. *J. Atmos. Sci.*, 34, 344-355.

Stauffer, D. R. and N. L. Seaman, 1990: Use of four-dimensional data assimilation in a limited-area mesoscale model. Part I: Experiments with synoptic-scale data. *Mon. Wea. Rev.*, 118, 1250-1277.

Stauffer, D. R. and N. L. Seaman, 1994: Multiscale four-dimensional data assimilation. *J. Appl. Meteor.*, 33, 416-434.

Stull, R. B., 1988: An introduction to boundary layer meteorology. *Kluwer Academic Publishers*, 666pp.

Sundquist, H., 1988: Parameterization of condensation and associated clouds in models for weather prediction and general circulation simulation. *Physically-based modelling and simulation of climate and climate change*, M.E. Schlesinger, Ed., Kluwer Academic Publishers, 433-461.

Thomas, S., C. Girard, G. Doms and U. Schätler, 2000: Semi-implicit scheme for the DWD Lokal-Modell. *Meteorol. Atmos. Phys.*, 75, 105-125.

Tiedtke, M., 1989: A comprehensive mass flux scheme for cumulus parameterization in large-scale models. *Mon. Wea. Rev.*, 117, 1779-1799.

Tiedtke, M., 1993: Representation of clouds in large-scale models. *Mon. Wea. Rev.*, 121, 3040-3061.

Wicker, L. and W. Skamarock, 1998: A time-splitting scheme for the elastic equations incorporating second-order Runge-Kutta time differencing. *Mon. Wea. Rev.*, 126, 1992-1999.

Xue, M., 2000: High-order monotonic numerical diffusion and smoothing. *Mon. Wea. Rev.*, 128, 2853-2864.

Yanai, M., S. Esbensen and J. Chu ., 1973: Determination of bulk properties of tropical cloud clusters from large-scale heating and moisture budgets. *J. Atmos. Sci.*, 30, 611-627.